KG^{2}B, a collaborative benchmarking exercise for estimating the permeability of the Grimsel granodiorite-Part 2: modelling, microstructures and complementary data

C David, J Wassermann, F Amann, J Klaver, Catherine Davy, J Sarout, L Esteban, E H Rutter, Q Hu, L Louis, et al.

KG²B, a collaborative benchmarking exercise for estimating the permeability of the Grimsel granodiorite: modeling, microstructures and complementary data

C. David[1], J. Wassermann[2], and the KG²B Team[3]*

[1]Université de Cergy-Pontoise, Laboratoire GEC, Cergy-Pontoise, France.

[2]Université de Cergy-Pontoise, Laboratoire L2MGC, Cergy-Pontoise, France.

[3]Complete list detailed in Appendix A.

Corresponding author: Christian David (christian.david@u-cergy.fr)

Key Points:

- A benchmarking exercise involving 24 laboratories was organized to estimate the permeability of the Grimsel granodiorite
- The microstructures of the Grimsel granodiorite were analyzed and quantified using BIB-SEM, micro-CT scanning, MICP and NMR techniques
- Permeability predictions from different models using microstructure data as input parameters are in good agreement with measurements

Abstract

A benchmarking exercise involving 24 laboratories was organized for measuring and modeling the permeability of a single low permeability material, the Grimsel granodiorite. To complement the data set of permeability measurements presented in a companion paper, we focus here on (i) quantitative analysis of microstructures and pore size distribution, (ii) permeability modeling and (iii) complementary measurements of permeability anisotropy and poroelastic parameters. BIB-SEM, micro-CT, MICP and NMR methods were used to characterize the microstructures and provided the input parameters for permeability modeling. Several models were used: (i) basic statistical models, (ii) 3D pore network and effective medium models, (iii) percolation model using MICP data and (iv) free-fluid model using NMR data. The models were generally successful in predicting the actual range of measured permeability. Statistical models overestimate the permeability because they do not adequately account for the heterogeneity of the crack network. Pore network and effective medium models provide additional constraints on crack parameters such as aspect ratio, aperture, density and connectivity. MICP and advanced microscopy techniques are very useful tools providing important input data for permeability estimation. Permeability measured ~orthogonal to foliation is lower that ~parallel to foliation. Combining the experimental and modeling results provides a unique and rich data set.

1. Introduction

Following a workshop on «The challenge of studying low permeability materials» that was held at Cergy-Pontoise University in December 2014, a benchmark exercise in which several laboratories estimate the permeability of a single material was proposed to the attendees. The selected material was the Grimsel granodiorite (Switzerland) and the benchmark was named the "KG²B" project, from "K for Grimsel Granodiorite Benchmark" (David et al., 2017). Multiple objectives were defined: (i) to compare the results for a given method, (ii) to compare the results between different methods, (iii) to analyze the accuracy of each method, (iv) to study the influence of experimental conditions (especially the nature of pore fluid), (v) to discuss the relevance of indirect methods and models, and finally (vi) to suggest good practice for low permeability measurements. The permeability measurements are presented in the companion paper. Here we will focus on item (v) and present the results of microstructure analyses and permeability modeling.

Fluid flow processes in rocks are controlled by the geometrical properties of pore and/or cracks and the topology of the pore/crack network. Linking permeability to microstructural properties has always been a challenge in rock physics. A first step is to acquire high quality data that allow thorough characterization of the pore space, preferably in 3D. As we are dealing with a crystalline rock, the focus is on cracks rather than pores. Cracks in rocks can be approximated as planar features with small width or aperture, randomly oriented or not in a 3D medium. Due to their limited resolution, optical microscopy techniques are not well-suited for the study of cracks. SEM studies have been commonly used to analyze cracks on thin-sections at high magnification. Ion beam milling is recommended to avoid biased interpretation of the microcrack morphology and statistics (Wong, 1982). Crack statistics provided by SEM studies can be from 2D analyses, from which 3D parameters (like crack surface per unit volume) can be inferred using stereology (Fredrich & Wong, 1986). Recent advances in ion polishing now allow improved images of pore structures and crack networks to be obtained using BIB-SEM (Klaver et al., 2015), or even 3D structures from FIB-SEM image stacks (Holzer et al., 2004). Wood's metal injection

into the pore space greatly enhance pore and crack detection and analysis on SEM images (Hu et al., 2012; Klaver et al., 2015). High resolution micro-CT techniques have become widely used to investigate the three-dimensional distribution of minerals and pores (Baker et al., 2012; Godel, 2013). With improvement of technology and analytical tools, sub-micron resolution can now be achieved with micro-CT imaging methods, but sometimes even this is insufficient to identify tiny cracks in crystalline rocks. One major advantage of micro-CT is that the technique is non-destructive and can be applied on centimeter scale plugs. Pore or crack size distributions can be obtained by image analysis on SEM images (2D analysis) or micro-CT reconstructed volumes (3D analysis), and also by conducting mercury injection capillary pressure (MICP) tests on small plugs. MICP is commonly used in petrophysical studies to obtain the throat size distribution and capillary breakthrough pressure by injecting mercury under increasing pressure (Hu et al., 2015). The throat size distribution given by MICP does not actually match the pore size distribution of the rock because of constrictions and ink-bottle effects in the pore space (Abell et al., 1999) but provides a first-order approximation that can be used in models. Other methods that provide insight into the pore size distribution include the gas adsorption (or BET) method (Schull, 1948) and NMR techniques (Josh et al., 2012).

Permeability models using microstructural data as input parameters have evolved since the pioneering work of Kozeny in the 1920s (Kozeny, 1927). A main challenge of all permeability models is to identify the characteristic length scale controlling permeability. This general statement rises from the permeability having the unit of squared length, but other factors like pore size variability and connectivity are also very important. Many different approaches have been proposed (Guéguen & Palciauskas, 1994). Originally based on the Kozeny-Carman equation (Kozeny, 1927), the equivalent channel model states that the characteristic length scale is the hydraulic radius, defined as the ratio between the pore volume and the pore surface area (Paterson, 1983; Walsh & Brace, 1984). In the equivalent channel model, permeability depends on bulk properties related to the pore space (volume to surface ratio, porosity, tortuosity - an ill-defined parameter related to the increased path length in a “tortuous” pore space) that, with the exception of tortuosity, are measurable at the sample scale. Statistical and effective medium models take advantage of the statistics of pore or crack geometries. For example, Gueguen & Dienes (1989) proposed a statistical model for crystalline rocks in which permeability depends on the mean crack aperture and radius, with cracks modeled as penny-shaped objects, on the average distance between cracks and on the fraction of connected cracks (which can be estimated from percolation theory). Only ensemble averages are estimated with limited input of the crack network topology. In contrast, network topology is taken into account in percolation and network models. For the percolation model proposed by Katz & Thompson (1986) the characteristic length scale is the so-called critical conductance (linked to a critical crack size), defined as the smallest conductance in the sample-spanning sub-network made of conductances larger than the critical conductance. The critical length scale can be obtained from the breakthrough pressure in MICP experiments using Washburn’s equation (Hu et al., 2015). Percolation models are supposed to work best when the pore size distribution is very wide. In heterogeneous porous media, preferential flow paths (with similar properties as the critical percolation subnetwork) are more likely to occur (David, 1993).

Pore network modeling has been widely used for permeability prediction (Bauer et al., 2012; Bernabé et al., 2003). In such models fluid flows in pipes or cracks forming the bonds of a 3D (or 2D) lattice with fixed topology (e.g. a cubic lattice). The geometrical properties of the conducting elements follow the pore/crack size statistics obtained by SEM analysis or

MICP (David et al., 1990). The flow equations are solved at each node and permeability is directly derived from Darcy's law, so does not depend on statistical averages (De Boever et al., 2012). Pore network modeling also allows the bond occupancy probability to be varied, so that networks with different average coordination number (or connectivity) can be considered for permeability estimation (David, 1993). Several of the permeability models mentioned above were tested by Casteleyn et al. (2011) on series of oolitic limestones from the Paris basin. Since the pore size distribution of these rocks was not very heterogeneous, hence statistical and network models were successful in matching the measured permeability, while the percolation model underestimated the permeability by about one order of magnitude.

One of the objectives of the KG²B benchmark was to conduct permeability modeling. Several models were selected by the participants. To achieve successful modeling, as discussed above, information is required about the rock microstructure (such as porosity, pore/crack aperture and length distribution, and connectivity). We will present the results of a thorough microstructural analysis and from NMR and MICP tests, as well complementary data on anisotropy and poroelastic parameters measured on a voluntary basis by some participants.

2. The KG²B Project: Summary

In total 30 laboratories from 8 different countries volunteered to participate in KG²B, and we received results from 24 laboratories that form the "KG²B Team". The complete list of participants who sent results is given in Appendix A. A dedicated website https:/labo.u-cergy.fr/~kggb/ was created with information on the benchmark, including a web page where the progress of the project could be followed on the "KG²B-wheel", which was updated as soon as results were received from any of the participants. It took one year to collect all of the results. In total we collected 45 permeability values, including 39 measured values and 6 results from modeling, on which this paper will focus. Statistical, network, percolation and effective medium models were used. We add a seventh modeling result in which a rock sample is treated as an RC (Resistance + Capacitor) low pass filter during pore pressure oscillation tests.

The Grimsel granodiorite was obtained from the Swiss Grimsel test site, a 450 meter deep Underground Research Laboratory (URL). The 950 meter long and 3.5 meter diameter tunnels were excavated in 1983 by a full face Tunnel Boring Machine (TBM) in hard rocks, mainly granite and granodiorite, at an altitude of 1730 m in the Central Aar Massif in Switzerland. The TBM excavation method limited perturbation of the host rock, with a quite small Excavation Damage Zone (EDZ) around the tunnel (Egger, 1989). Along the tunnel, major damage zones are located in meter scale shear zones or widely spaced discontinuities caused by regional deformation. Two cores of Grimsel granodiorite, each about one meter long and of diameter 85 mm, were provided by our Swiss colleagues in September 2015. These cores were retrieved at a distance of 4 to 6 meters from the tunnel of the Grimsel test site, far away from the EDZ influence. The cores were cut into small blocks at lengths requested by each participant (between 2 and 10 cm). A grain shape foliation is visible on the cores at an angle of about 20-30° with respect to the core axis. The foliation is related to compositional banding of alternating dark biotite layers and quartz-rich layers (Schild et al., 2001). Natural and induced cracks have been observed in past studies (e.g. Smith et al., 2001). In particular there is a natural interconnected network of cracks producing about 1%

porosity in the granitic matrix. Stress release due to drilling and sample preparation outside the URL seems to be responsible for larger micro-crack apertures than those observed directly in situ (Schild et al., 2001). As some laboratories provided permeability measurements in directions other than that required of the participants (i.e. the core axis direction), we will also discuss the permeability anisotropy.

The detailed analysis of the permeability measurements is given in the companion paper. Let us recall the most important results. For the whole data set of 39 measurements, the average permeability was 1.47 10^{-18} m²; however 4 outliners were identified and removed, leading to an average permeability of 1.11 10^{-18} m² and a standard deviation of 0.57 10^{-18} m². A striking result was the large difference between measurements using gas or liquid as the pore fluids: the permeability to gas was about twice as large as the permeability to liquid (k_{gas}=1.28 10^{-18} m², k_{liquid}=0.65 10^{-18} m²). The model predictions presented in this paper will be compared to those values.

We will use the same convention as in the companion paper for presenting the data set. Each lab was assigned a number in increasing order with respect to the distance between their sample and the tunnel. Lab#01 worked on the sample closest to the tunnel, and Lab#24 on the farthest sample.

3. Microstructure and porosity analyses

3.1. Quantitative Microstructural Analysis

Here we describe efforts to determine the main fluid flow pathways at the centimeter scale, which is the relevant scale for the laboratory experiments. To this purpose, several direct imaging methods were used: automated optical microscopy of thin-sections, and Broad Ion Beam/Scanning Electron Microscopy (BIB-SEM) of intact or Wood's Metal (WM) impregnated samples.

3.1.1 Methods

Two adjacent blue dye impregnated thin-sections of standard size were prepared perpendicular and parallel to the core axis from the original core sample (Figure 1). Thin-sections were automatically scanned with the Virtual Petroscan (ViP) (Schmatz et al., 2010) in plane polarized and crossed polarized light (PPL and XPL). Porosity was segmented from the PPL image map (approximately 20,000 * 12,000 pixels, pixel size of 1.4 µm i.e. 2.8 cm * 1.68 cm ≈ 4.7 cm^2) by unsupervised iso-cluster classification and re-grouped into porosity and matrix based on visual inspection followed by a boundary cleaning operation (dilation), all in ArcGIS 10.

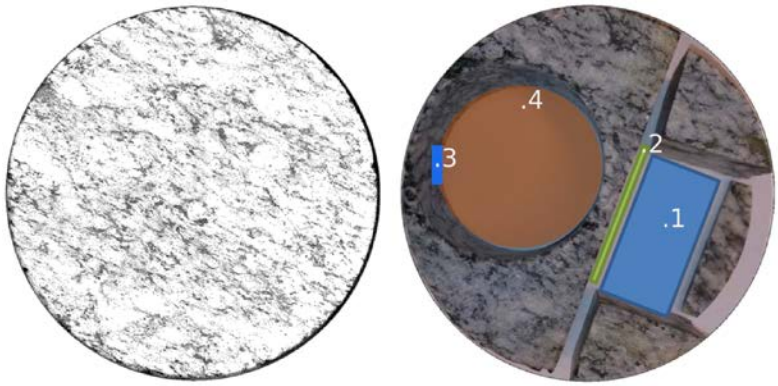

Figure 1. Grimsel granodiorite core (left) and sampling (right) for thin sections perpendicular (1), and parallel (2) to the core axis, for BIB-SEM and WM (3), and plug for permeability measurements for Lab#23 (4).

From the same core sample, one subsample was prepared by BIB polishing to investigate the microstructure by SEM. Details on this technique are given by Klaver et al. (2012). Four areas were mapped at high resolution (10,000 – 20,000 x magnification) for quantitative analyses of the pore space. Porosity was segmented by a seed-and-grow algorithm (Jiang et al., 2015) and manually corrected where needed. Pore spaces with circularity below 0.2 and an axial ratio above 3 were automatically classified as cracks (including grain boundary cracks). Average crack intensity (expressed in crack number/m) and average crack thickness were calculated based on each pixel row from every map.

Another sub-sample was injected at 500 MPa with Wood's metal (WM), which is a non-wetting alloy with wetting properties similar to mercury and which solidifies at room temperature. This method resembles Mercury Intrusion Porosimetry (Klaver et al., 2015). We expected insignificant damage to the pores due to the material strength.

3.1.2 Visible porosity and pore size distributions

Over 60,000 pores were segmented from the thin-sections and the largest pores were approximately 0.3 millimeter in equivalent diameter (Figure 2). The thin-sections show different visible porosities: 0.71% and 1.55% for the parallel and perpendicular sections, respectively. This difference most likely occurred because the thin-sections are not wholly representative at the centimeter scale regarding porosity. Alternatively, this contrast may owe to highly anisotropic pore shapes with large pore diameters parallel to the section and small diameters perpendicular to the section.

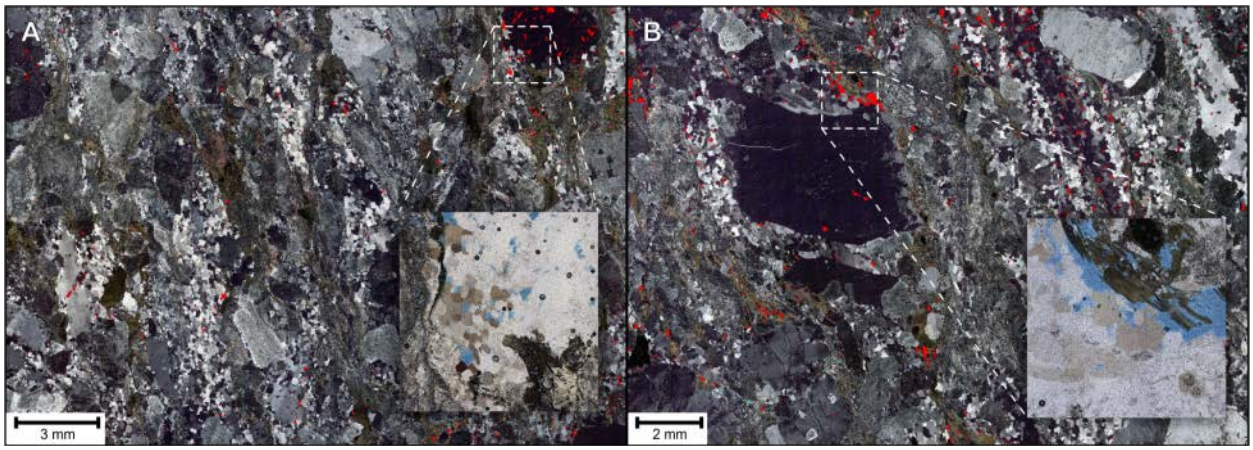

Figure 2. ViP XPL maps overlain by pore segmentation in red of the parallel thin-section (A) and perpendicular thin-section. The insets show the blue dye filled pores in PPL.

From SEM, the weighted average porosity in segmented maps perpendicular to the core direction is 0.45% with a porosity of 0.54%, 0.16%, 0.64% and 0.39% in maps A, B, C and D, respectively (Figure 3A-D). However, most of the pore space (average 0.36%) is associated with cracks, indicated in red in the figure. In map D, no cracks were counted, and all pores are interpreted as isolated pores within a single phase consisting mainly of K, Si, Al (Figure 3E) and interpreted as K-feldspar. Other pore space-mineral associations are: 1) cracks at grain boundaries and within biotite (Fe, K, Mg, Al, Si); 2) minor pores and cracks along albite/plagioclase (Na/Ca, Al, Si) grain boundaries; 3) pores and cracks at quartz (Si, O) grain boundaries and fluid inclusions; and, 4) fluid inclusions in apatite (Ca, P).

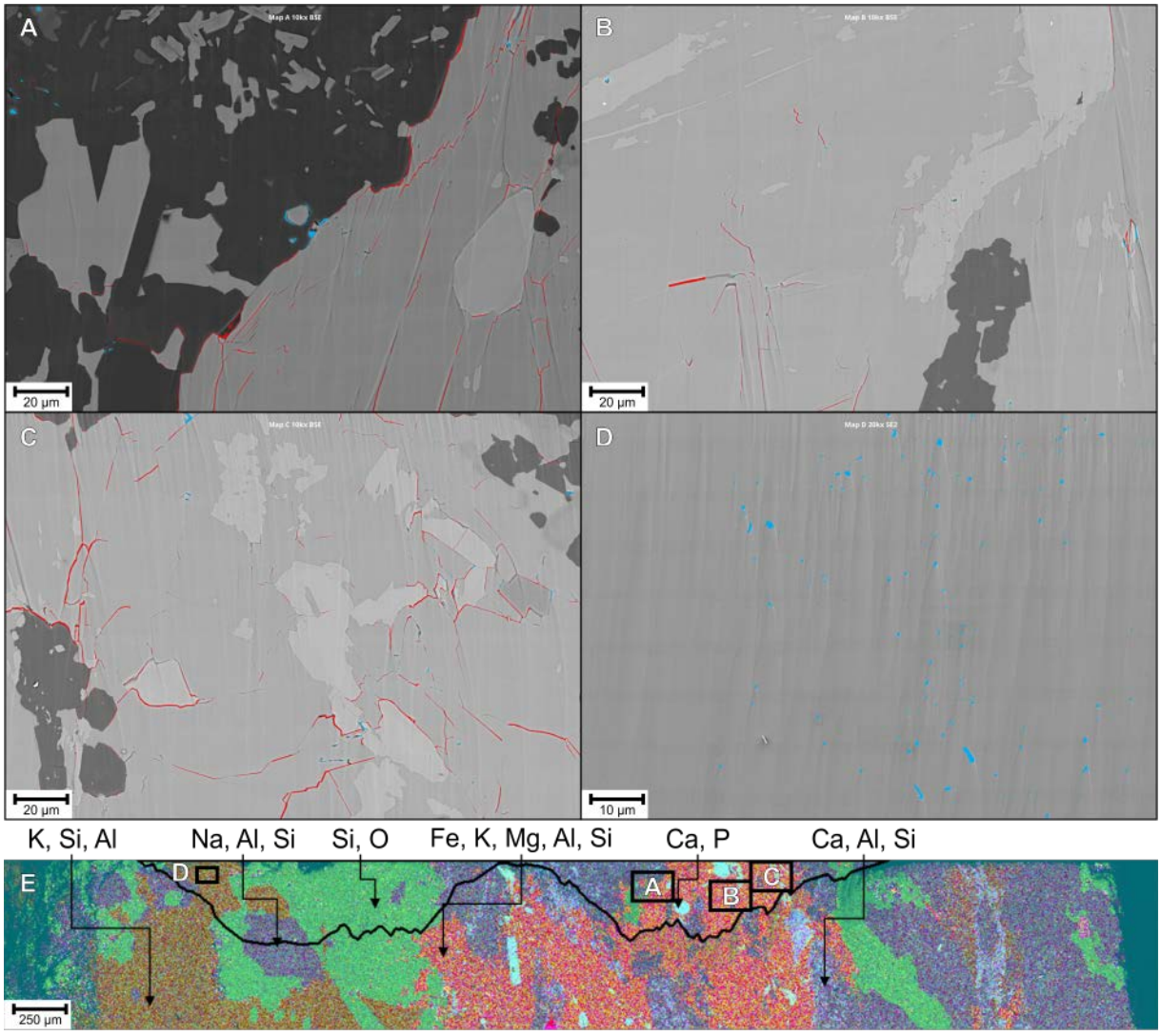

Figure 3. Backscattered Electron (BSE) image maps with pore space segmentation of maps A-D. Interpreted cracks are in red and pores in cyan. The EDS (Energy Dispersive Spectroscopy) overview map shows the locations of the maps with respect to BIB cross-sections and elemental compositions (E).

The pore size distributions (PSDs) of the imaged thin-sections show a clear increase in pore frequency with decreasing equivalent diameter to about 6 µm (Figure 4A). The PSDs of the BIB-SEM maps show a clear peak at 200 - 300 nanometer equivalent diameter and another apparent increase below 100 nanometers. These smaller segmentations are below 18 pixels in size. They are interpreted as noise and hence excluded from the analyses in Figure 4B, which

shows normalized frequencies (number of pores divided by the imaged area and bin width). Taking into account both pores and interpreted cracks, only maps B and C show comparable best fits. The fact that the normalized PSDs do not show uniform best fits indicates that pore space may have been underestimated due to the large grain sizes and other heterogeneities. Considering only the interpreted cracks in red (Figure 3A-D), the average crack thickness is 283 nm, within the visible range in Figure 4A. The average crack intensity over maps A-C is 14749 cracks/m.

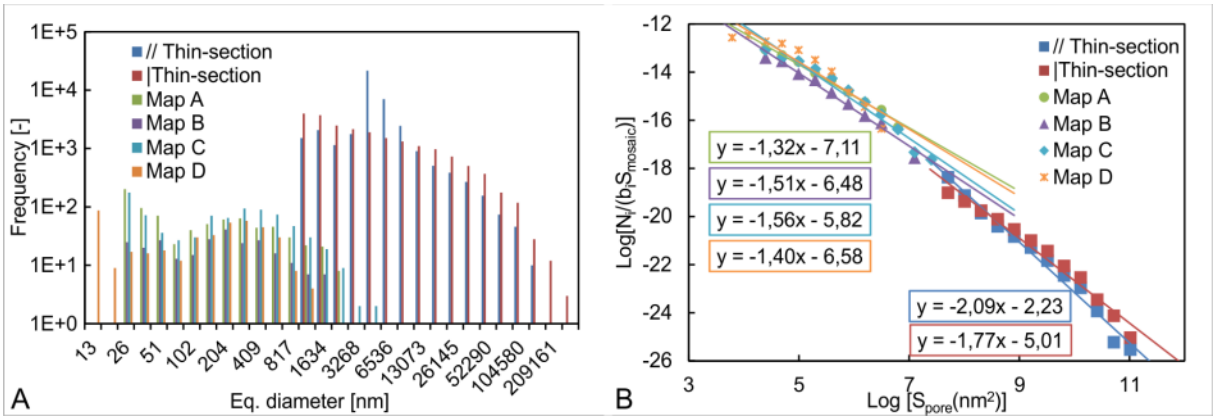

Figure 4. A) PSDs of segmented porosity in the thin-sections and BIB-SEM maps. B) Plot showing the PSDs, normalized over the imaged area for all segmented pores above 18 pixels in size, i.e. 6.5 µm, 144 and 72 nm for the thin-sections, map A-C and map D respectively.

3.1.3 Pore connectivity

The WM-filled cross-section is shown in Figure 5; the minerals are mostly biotite, albite, plagioclase and quartz (Figure 5A). Most of the WM is located in the cracks. Most of the WM-filled cracks seem to be associated with biotite (Figure 5B), and have widths of approximately 0.2-1 µm (Figure 5C).

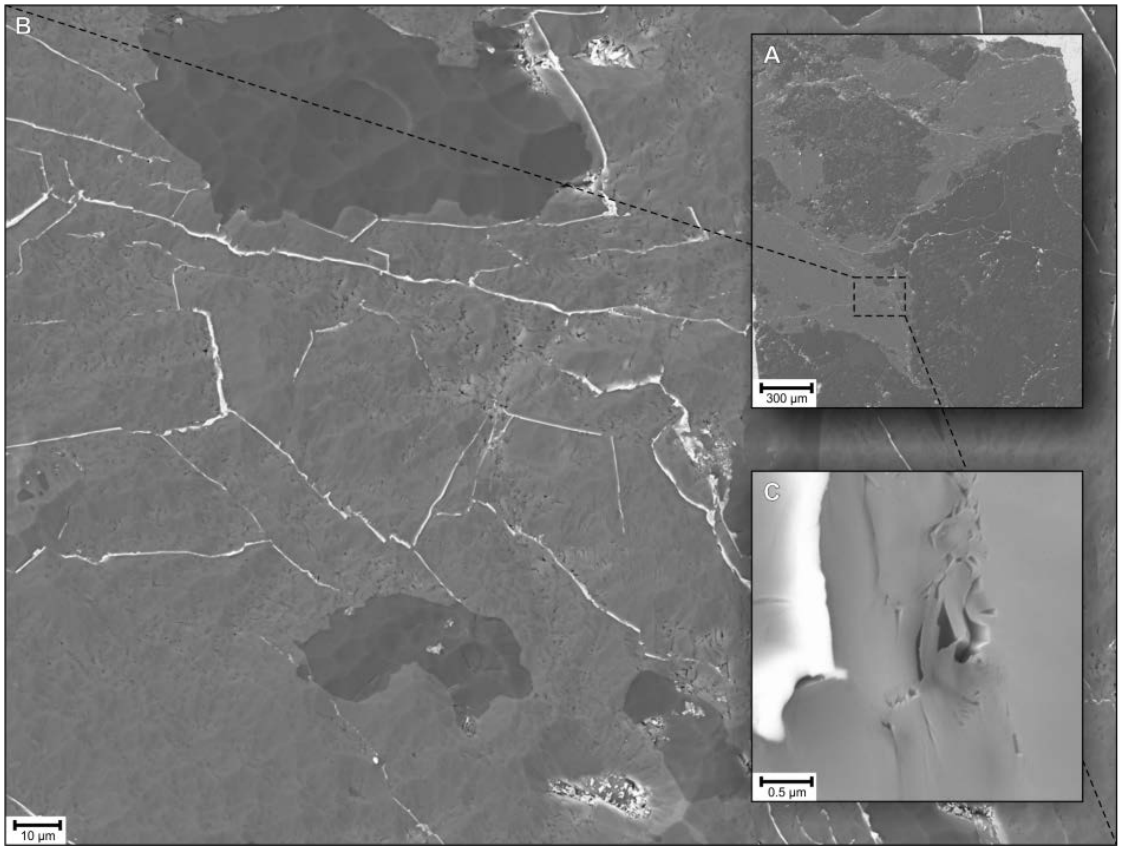

Figure 5. (A) Overview BSE image showing the WM intrusion (in white) at the sample scale. (B) Higher definition image map of the biotite dominated area shows connected crack networks in 2D. (C) WM-filled crack 200 nm in width next to isolated pores.

3.1.4 Synthesis of microstructural analysis

Macroscopic investigation reveals minerals of several centimeters in size, indicating that microstructural investigations limited to two adjacent thin-sections are most likely not representative of porosity at the centimeter scale. The variability in porosity at the thin-section scale is significant (with values of 0.71% and 1.55%). However, the expected order of magnitude of porosity (about 1%) is attained. A greater number of realizations would be necessary to achieve representativeness in a statistical sense.

In addition ViP- BIB-SEM investigations provided PSDs, enabling comparison with bulk measurements, and revealed pore-mineral associations which can help with up-scaling scenarios. Most of the pore space is visible with optical microscopy, indicating that the relevant pores for storage are in the sub-millimeter to micrometer range. However, the pore connections are most likely in the submicron range as indicated by the BIB-SEM investigations, which revealed significant cracks and grain-boundary features in that range. The WM-BIB-SEM investigations also indicate that crack flow is the most important transport process. The WM-filled cracks tend to be wider and are connected in 2D, perhaps opened due to the high pressures (while closing smaller cracks). This hypothesis is the subject of ongoing research.

This analysis is complemented by simplified calculations of permeability in Section 4, which assume that biotite is the main contributor to fluid flow, and that at room conditions the rock has an average porosity of 0.45%, a crack aperture of 283 nm, and a crack density of 14749 cracks/m. These estimates provide insights into the key factors controlling the transport properties and flow paths identified by microscopy.

3.2. Microstructure study using micro-CT

A micro-tomography study was conducted at CSIRO Perth on a small sample of Grimsel granodiorite with 4 mm diameter and 10 mm length. The micro-CT equipment is the XradiaTM Versa microtomography system (XVRM126). This system is composed of an X-Ray source, a rotating sample holder and an X-Ray detection system. The source is generated by the impact of a focused beam on a thin target; the spot size can vary from 1 to 5 µm depending on the operating conditions. The diverging geometry of the X-Ray results in a magnification of the object. The X-Ray source used allows application of voltage and power ranges from 40 to 160 kV and from 4 to 10 W respectively. The X-Ray detector comprises several lenses mounted on a turret and the detector itself picking up X-Ray images of the sample. The mounted lens ranges from magnification level 0.4X to 40X covering resolutions from few tens of µm to 0.7 µm in optimal conditions. The latter resolution can be obtained on 5 mm diameter samples. The images are generated by acquisition of a set of radiographs, while rotating the sample stepwise through a 360° rotation. For the present study, the voxel size was 5 µm, enough to identify tiny pores (as shown also in BIB-SEM analysis) but insufficient to see the cracks, which have thicknesses dominantly in the sub-micron range. In Figure 6a, four density maps with grey-scale coding are shown on cross-sections at different heights from top to bottom. The brighter areas correspond to denser minerals. Clearly the rock appears very heterogeneous from the mineralogical viewpoint. The foliation oriented from left to right on the images is visible. Magenta circles highlight the presence of tiny, probably isolated pores, as discussed in the BIB-SEM section. 3D reconstructions of the sample are shown in Figure 6b. Again heterogeneity is ubiquitous. The reconstructions confirm that, at this scale, the investigated volume is below the REV (as discussed in the companion paper). The pore space reconstruction (excluding cracks) shows that the tiny pores are isolated and should not contribute significantly to macroscopic flow, unless connected through the crack network. Generally the pores are uniformly distributed in the rock, although clusters are sometimes observed (Figure 6b). As mentioned in the BIB-SEM analysis, fluid flow is controlled by a 3D network of cracks that is mostly located at grain boundaries or within biotite. Indeed such cracks not visible at the micro-CT scale were filled with Wood's metal (Figure 5) after WM injection.

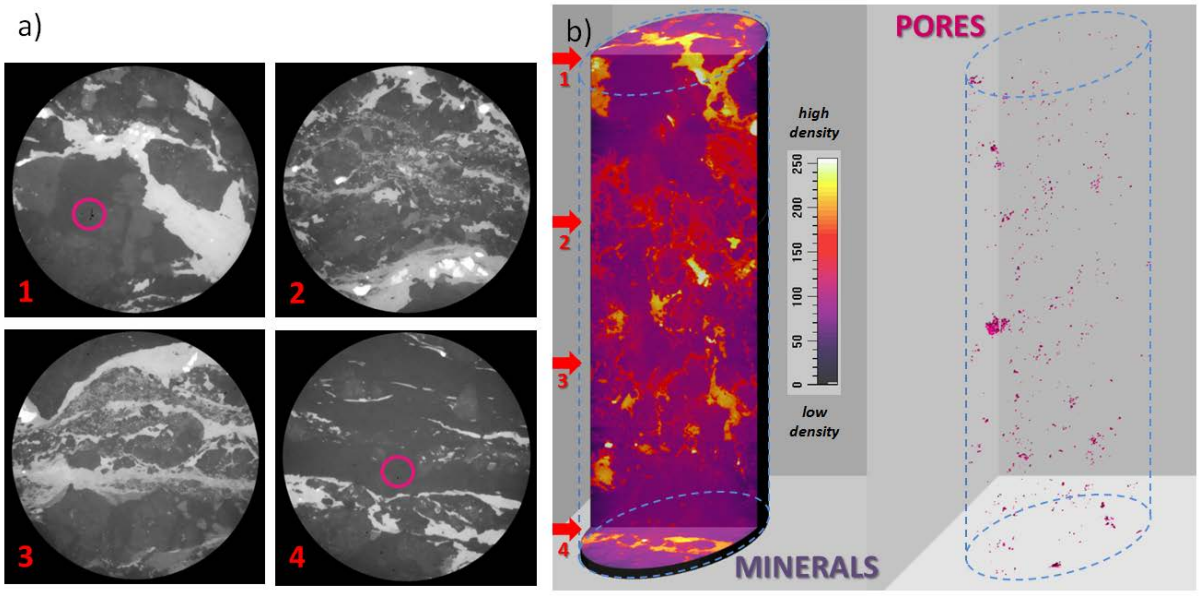

Figure 6. Micro-CT scan analysis of a small sample of Grimsel granodiorite (diameter 4mm, length 10 mm). a) Four sections at different heights from top to bottom; the pink circles highlight some pores (black spots). b) Left, 3D reconstruction of the matrix density map (8 bits color coding), with red arrows indicating locations of the four cross-sections; right, 3D map showing isolated or clustered tiny pores. The cracks evidenced by BIB-SEM analysis could not be resolved by this technique.

3.3 Pore Structure Analysis with MICP and NMR

Mercury injection capillary pressure (MICP) can be used to measure pore structure characteristics such as total pore area, bulk density, porosity, pore throat distribution, permeability and tortuosity (Hu et al., 2015). Liquid mercury, which has a high surface energy and is non-wetting, is forced into the pore space under increasing capillary pressure. As mercury pressure increases, smaller pore throats are invaded. Mercury will only invade a pore throat when a sufficient mercury pressure, inversely proportional to the throat diameter is applied (Gao & Hu, 2013). This is expressed through the Washburn equation, which assumes a cylindrical pore shape (Washburn, 1921). For a 1cm long cubic sample a typical MICP test takes 3-4 hours to complete, with measurable pore-throat size ranging from 3 nm to 36 µm for low-porosity (<5%) samples. Figure 7 shows the results obtained from MICP on the Grimsel granodiorite.

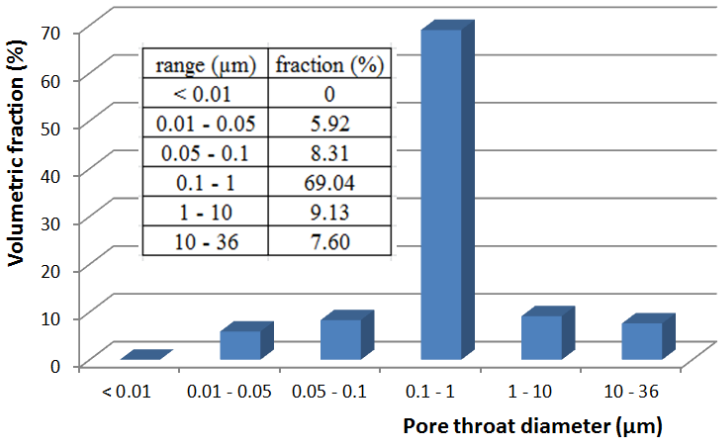

Figure 7. Throat size distribution derived from MICP on the Grimsel granodiorite.

The porosity provided by the mercury injection test at the highest capillary pressure is 0.59%, lower but close to the average porosity found by other teams using different techniques (0.77%). This is probably linked to the smaller size of the MICP plug compared to the permeability samples. A very strong peak is observed on the histogram, corresponding to a pore throat radius in the range between 0.1 and 1 µm.

In Figure 8 we present the results of NMR spectroscopy conducted on five small plugs (diameter 25 mm, length 22 mm) saturated with water under vacuum and 13 MPa hydrostatic pressure, using a 2 MHz GeoSpec2 from Oxford-GIT Ltd. Low-field proton NMR provides the transverse relaxation time T_2 from which bulk and bound water distributions can be extracted (Dillinger & Esteban, 2014). For the saturated state (Figure 8a), the results are very consistent, with one strong peak at T_2=0.15 ms and two weakest ones in the range 10 - 100 ms. Short relaxation times usually correspond to bound water (e.g. capillary pore sizes and clay bound water) and long relaxation times correspond to free (or mobile) water; Figure 8 shows that, in the Grimsel granodiorite, most of the water in the pore space is bound water at 13 MPa hydrostatic pressure.

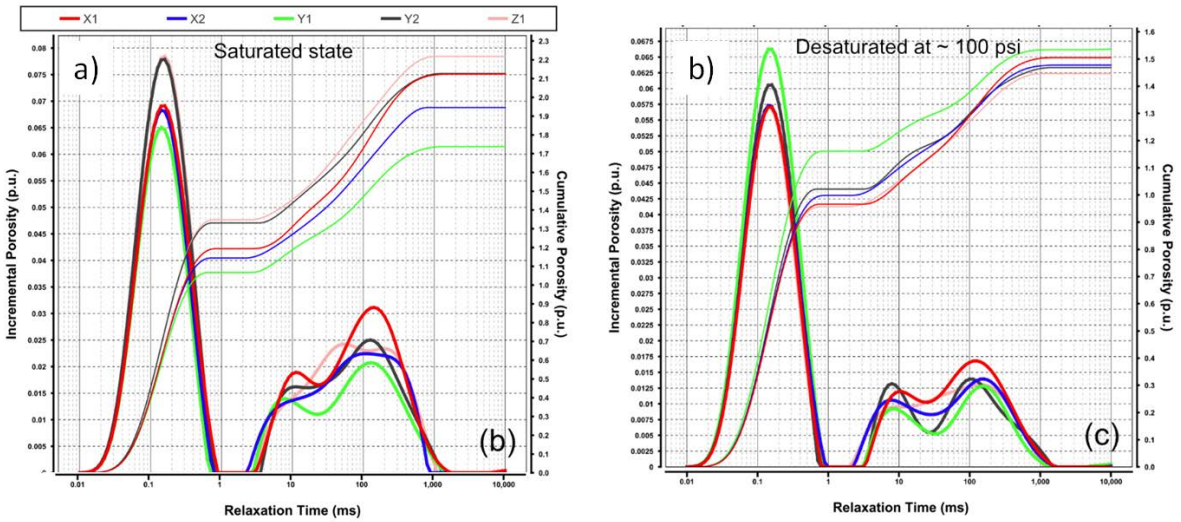

Figure 8: NMR transverse relaxation time T_2 spectra and associated cumulative porosity in five small core plugs of Grimsel granodiorite (a) under water saturated conditions, and (b) a desaturated state at ~ 6.9 bars.

For these five plugs the NMR porosity ranges from 1.75 to 2.2 % (average 2.03 %) which agrees with the range found with direct measurements (see next section). The five samples were also desaturated by centrifuge to achieve an equivalent capillary pressure of ~ 6.9 bars, and NMR measurements were repeated (Figure 8b). Such experiments allow one to evaluate the relative amount of mobile water and irreducible water. Note that sample Y1 has a different behavior than the others.

3.3. Porosity measured on plugs

We collected 35 porosity values using different methods (helium pycnometry, triple weight method, mercury injection, NMR). As with permeability, no systematic trend was found when plotting porosity values as a function of the distance to the tunnel (Figure 9a). However more consistent values seem to occur in the first eighty centimeters. The average porosity is 0.77% (Figure 9b) with a standard deviation of 0.36%.

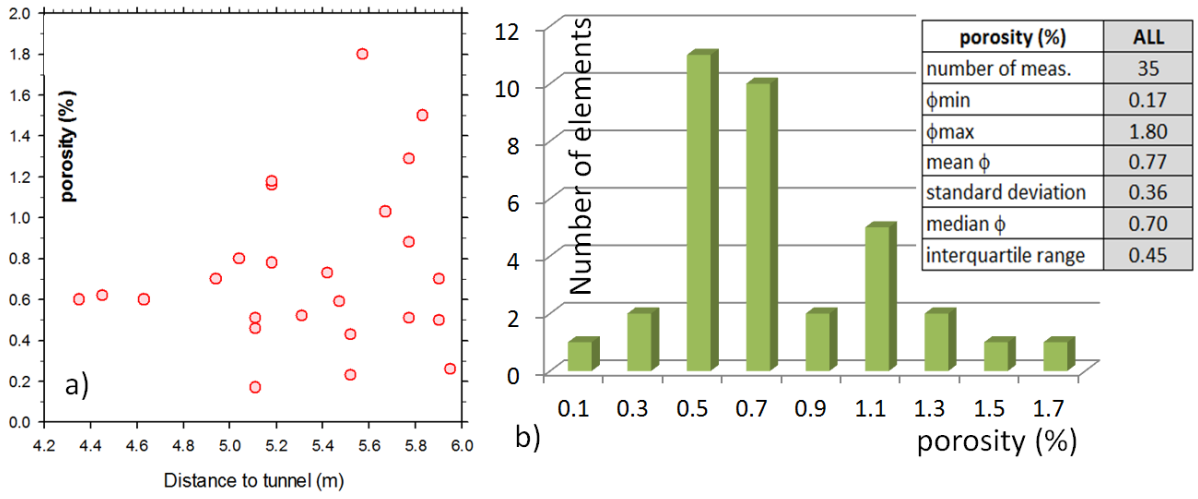

Figure 9. a) Porosity vs. distance to the tunnel. b) Statistics of porosity measurements on plugs.

These values measured on macroscopic samples are in good agreement with those derived from thin section analyses reported in section 3.

4. Permeability Estimation from Models

About 13% of the permeability estimates collected during the benchmarking exercise were obtained from model predictions. Several models have been used and can be classified as statistical, percolation, free-fluid, pore network and effective medium models. In addition, we propose a model based on the analogy with an RC filter circuit to interpret the results from pore pressure oscillation experiments.

4.1 Permeability Estimation from Statistical Models

Past research on natural or artificial geo-materials (Scherer et al., 2007; Song et al., 2015) has shown that the order of magnitude of fluid permeability may be assessed with simple statistical models. This requires a number of assumptions, the first being that the fluid does not interact with the solids.

The pore network in a crystalline rock can be approximated by a 3D array of orthogonal flat cracks with constant length and aperture $2w$ (w is defined hereafter as the half aperture). The pore space in the Grimsel granodiorite is considered with such model, in which the aperture is replaced by the average crack width obtained from the BIB-SEM analysis. The simplest model derived from Poiseuille's law for flow into straight parallel cracks gives:

$$k = \phi\, w^2/3 \tag{1}$$

In real materials, the pores are non-circular, intersecting and tortuous, so that the equation above is oversimplified (Scherer et al., 2007). The BIB-SEM results in Section 3 yielded an average porosity ϕ=0.45% and average crack aperture $2w$=283 nm or 1 µm. This provides a permeability prediction of $3\ 10^{-17}$ m^2 if the main pore width is 283 nm, and $3.7\ 10^{-16}$ m^2 if the main pore width is 1 µm. As shown earlier, the order of magnitude of measured permeability for the Grimsel granodiorite is 10^{-18} m^2. This suggests that the main pore size for transport is sub-micrometric, rather on the order of 283 nm, taking into account that the permeability measurements were done at 5 MPa effective pressure whereas the porosity measurements were done on unstressed rock.

Alternatively, permeability can be estimated by a fracture-based relationship for laminar flow (Zimmermann et al., 2005):

$$k = 2\lambda_L\, w^3/3 \tag{2}$$

where λ_L is the linear frequency of fractures or cracks. Taking λ_L =14749 m^{-1} and again $2w$ =283 nm results in a predicted permeability of $2.8\ 10^{-17}$ m^2. However, considering that most of the cracks relevant for flow are associated with biotite, and assuming a biotite content of 40%, the predicted permeability based on crack density is $1.1\ 10^{-17}$ m^2 (i.e. $11\ 10^{-18}$ m²), in agreement with the prediction of the previous model. This value is also larger than the average measured permeability by one order of magnitude, but again corresponds to the unstressed rock.

Although this analysis is quite simplistic, it provides useful insights into the location of fluid pathways and relates permeability measurement to microstructure quantification. Further

analysis could be done by 3D pore quantification and modeling, as done by (Song et al., 2016) for a tight sandstone (with crack-like pores). Such analyses allow us to assess the contributions of different pore (crack) sizes to transport, material anisotropy, and the effect of stress on permeability variations.

4.2 Permeability Estimation from Pore Network Modeling

Permeability simulations were conducted using a 3D pore network model (PNM) described in Casteleyn et al. (2011). The input data required for such modeling include (i) an analytical description of the pore (or crack) size distribution, (ii) the average pore (or crack) shape, and (iii) the rock porosity. In the Grimsel granodiorite, fluid flows through a network of cracks with low aspect ratio (Figure 5). In the PNM simulation, fluid flows through a network of pipes with elliptical cross-section. For sake of simplicity all the pipes have the same aspect ratio ξ and constant length L_P (David, 1993). MICP provides an estimate of the crack aperture distribution (equivalent to the throat size diameter in Figure 7) which corresponds to the minor axis $2w$ of the elliptical pipes in the model; the semi-major axis R given by $R=w/\xi$ in the model corresponds to the half-width of the cracks. The local conductance of each bond is given by $\pi w^4/(4L_P\xi(1+\xi^2))$ (David, 1993). The experimental crack aperture distribution (Figure 7) is modelled by a log-normal distribution in the range (0.01µm, 30µm) with a peak centered at 0.5µm. The PNM is a cubic lattice with 20 nodes in each direction (Figure 10); the pipes are located at the branches of the lattice. An algorithm generates as many aperture values as pipes in the network (about 24000), following the log-normal distribution. These aperture values are randomly assigned to the pipes in the network. The constant pipe length is derived from the "network porosity" which must match the rock porosity. For sake of simplicity the network porosity was fixed at 1%, close to the average porosity value measured on plugs. Fluid flow is simulated by imposing a constant pressure gradient across any pair of opposite faces of the network (David et al., 1990) and the permeability is derived from the net flow rate at the outlet face using Darcy's law. The whole process is repeated 10 times to obtain an average permeability and standard deviation. Several simulations were conducted for three different values of the aspect ratio in the range ξ=0.001, 0.01 and 0.1 (Figure 10). The simulations were done for different bond occupancy ratios until permeability fell to zero (the percolation threshold); this can be achieved by randomly removing pipes in the network until a selected value of bond occupancy is achieved.

The results of PNM simulations show that (i) permeability decreases when the fraction of pipes in the network decreases, with a sharp fall near the percolation threshold (0.25 for a cubic lattice), (ii) permeability is the same in all three directions within numerical errors, and (iii) permeability is not changed by the pipe aspect ratio. This last result shows that permeability is essentially controlled by the crack aperture distribution which is the same in all simulations. For 100% bond occupancy, the coordination number is equal to 6 and the network permeability is 28 10^{-18} m². Such a high coordination number (and permeability) is probably much too high for the Grimsel granodiorite.

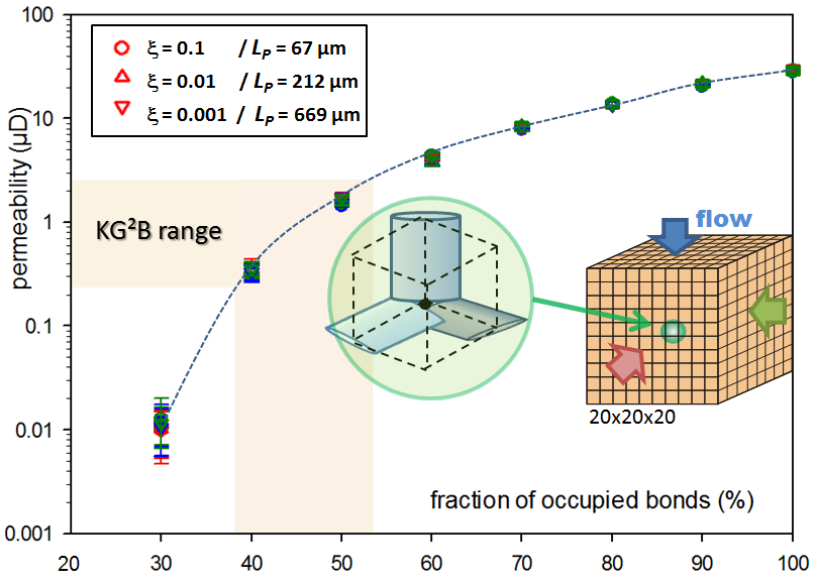

Figure 10. Results of permeability simulation using a 3D pore network model on a 20x20x20 cubic lattice. Cracks are represented by pipes with elliptical cross-sections with minor axes derived from MICP data, constant aspect ratio and constant length. Three aspect ratios were considered: 0.1 (circles), 0.01 (upward triangles) and 0.001 (downward triangles). Colors red, blue and green define the directions in which permeability is calculated. Error bars correspond to the standard deviation of permeability values for 10 network realizations with the same statistical properties.

The experimental permeability range found in the benchmarking exercise is highlighted in Figure 10. This range is consistent with a fraction of occupied bonds between 38% and 53%, thus a mean coordination number probably lower than 3, a reasonable value for a hard rock in which crack connectivity is expected to be low. The crack network in Figure 5 suggests an average coordination number close to 3, although it is hard to imagine what the real 3D coordination number is from 2D images. Given the crack lengths observed in Figure 5 (tens of micrometers) and the PNM results (Figure 10), our simulations suggest that the crack aspect ratio should range between 10^{-1} and 10^{-2}. As we tried to match the permeability measured at 5 MPa effective pressure, the inferred microstructural properties (aspect ratio and coordination number) correspond to that of the stressed rock.

4.3 Permeability Estimation from Effective Medium Modeling

Based on the microstructural data available, the Grimsel granodiorite is modeled as a homogeneous and isotropic solid, an aggregate of randomly oriented and naturally fused grains containing randomly oriented and spaced micro-cracks with finite diameter $2R$ and aperture $2w$. The number of micro-cracks per unit volume is N_V, and their aspect ratio is $\xi = w/R$. For sake of simplicity, the micro-cracks are modeled as oblate ellipsoids (thin cracks with $\xi << 1$). They can overlap/intersect so as to allow hydraulic connectivity and fluid flow through the rock at the macroscopic scale. The theoretical porosity of such a medium is given by Garboczi et al. (1995):

$$\phi = 1 - e^{V_C N_V} \tag{3}$$

where V_C is the volume of a single ellipsoidal micro-crack,

$$V_C = \frac{4}{3}\pi\xi R^3 \tag{4}$$

In this context, the crack density $\rho_V = N_V R^3$ is (Sarout, 2012; Walsh, 1965)

$$\rho_V = -\frac{3}{4\pi\xi}\log(1-\phi) \tag{5}$$

Let us assume that the network of micro-cracks in the Grimsel granodiorite is well above the hydraulic percolation threshold and that this network is the sole source of permeability (no background porosity). In this case, the permeability of the rock can be modeled using the concept of hydraulic radius (Gueguen & Dienes, 1989)

$$k \sim \alpha\phi m^2 \tag{6}$$

where $m = V_C / S_C$ is the hydraulic radius of ellipsoidal micro-cracks defined as their volume-to-surface ratio; and α is a dimensionless parameter derived from Poiseuille's law, related to the geometry of the hydraulically conducted network of micro-cracks, of the order of $\alpha \sim 1/3$ for a network of ellipsoidal micro-cracks (Sarout, 2012). The effective permeability of this cracked medium is explicitly related to its micro-structural parameters by (Sarout, 2012; Sarout et al., 2017)

$$k_{eff}(\phi,\xi,R) = \frac{16}{27}\frac{\phi R^2\xi^2(1-\xi^2)}{2\sqrt{1-\xi^2}+\xi^2 log\left(\frac{2-\xi^2+2\sqrt{1-\xi^2}}{\xi^2}\right)} \tag{7}$$

This simple model explicitly relates the effective permeability of the micro-cracked rock to the crack porosity ϕ, the crack aspect ratio ξ and radius R or, equivalently, to the crack density ρ_V, ξ, and R (Figure 11). This is because ϕ and ρ are related through equation (5) once the geometry of the cracks is set in the micro-structural model (oblate ellipsoids with $\xi << 1$).

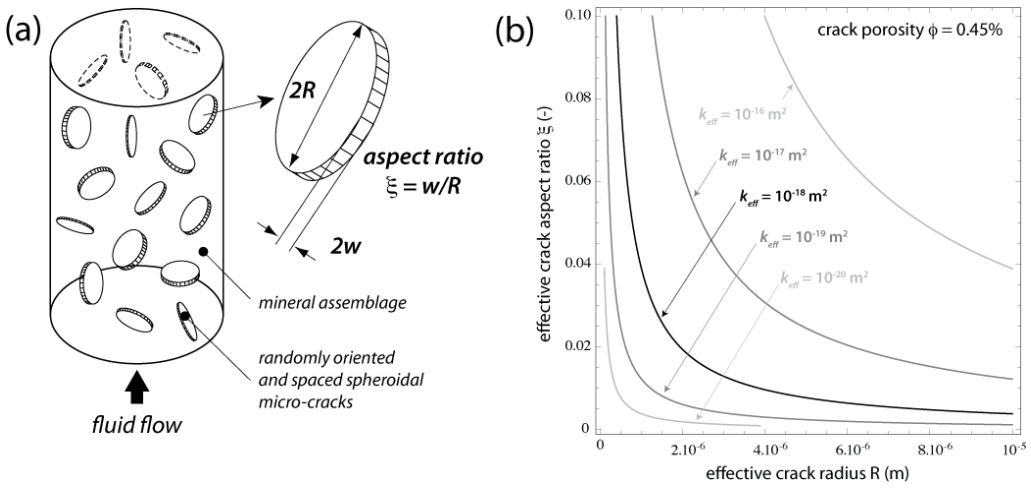

Figure 11. (a) Microstructural model of the Grimsel granodiorite. (b) Effective permeability predictions as a function of crack porosity, effective aspect ratio, and crack radius.

The experimental and microstructural parameters derived from measurements are the following:

- Measured average permeability @ P_{eff} = 5 MPa: 0.6 10^{-18} m² (liquid) to 1.3 10^{-18} m² (gas)
- Permeability extrapolated to P_{eff} = 0 MPa (room conditions): k_{exp} = 1 to 5 10^{-18} m²
- Measured porosity @ P_{eff} = 0 MPa: ϕ_{exp} = 0.8% (cracks only)
- Porosity from microstructure @ P_{eff} = 0 MPa: ϕ_{micro} = 0.45% (cracks only)
- Crack half-aperture @ P_{eff} = 0 MPa: w_{micro} = 140 nm
- Linear crack number density @ P_{eff} = 0 MPa: $\lambda_{L\text{-}micro}$ = 14749 m^{-1}

One model parameter can be inferred from these data, the volumetric crack density ρ_V defined in equation (5) which is related to the surface crack number density λ_A through the average of their squared crack radius $\langle R^2 \rangle$ (Hadley, 1976)

$$\rho_V = \frac{3}{4\pi}\lambda_A \langle R^2 \rangle \tag{8}$$

The linear and surface crack number density are related through *(Zimmermann et al.*, 2005)

$$\lambda_A = \frac{\pi}{2}\frac{\lambda_L}{\langle R \rangle} \tag{9}$$

Combining equations (8), (9) and (5) yields

$$\rho_V = \frac{3}{8}R\lambda_L \;\; and \;\; \phi(\lambda_L, \xi, R) = 1 - e^{-\frac{1}{2}\pi R \xi \lambda_L} = \phi(\lambda_L, w) = 1 - e^{-\frac{1}{2}\pi w \lambda_L} \tag{10}$$

so that the permeability in equation (7) can be rewritten as

$$k_{eff}(\lambda_L, \xi, w) = \frac{16}{27}\frac{w^2(1-\xi^2)}{2\sqrt{1-\xi^2}+\xi^2 log\left(\frac{2-\xi^2+2\sqrt{1-\xi^2}}{\xi^2}\right)}\left(1 - e^{-\frac{1}{2}\pi w \lambda_L}\right) \tag{11}$$

The data inversion strategy consists of the following steps:

1. Using equation (7), and the measured porosity ϕ_{exp} and permeability k_{exp}, we first define the effective crack radius function $R_{sol}(\xi)$ satisfying $k_{eff}(\phi_{exp}, \xi, R_{sol}(\xi)) = k_{exp}$,

$$R_{sol}(\xi) = \frac{3}{4}\left[\frac{3k_{exp}}{\phi_{exp}\xi^2(1-\xi^2)}\left[2\sqrt{1-\xi^2} + \xi^2 log\left(\frac{2-\xi^2+2\sqrt{1-\xi^2}}{\xi^2}\right)\right]^2\right]^{1/2} \tag{12}$$

2. Noting that by definition $R_{def}(\xi, w) = w / \xi$, we equate $R_{sol}(\xi) = R_{def}(\xi, w_{sol})$ and determine the effective crack half-aperture w_{sol} so that this equality is satisfied for all aspect ratios ξ.

3. Using equation (10), and noting that $\phi(\lambda_{L\text{-}sol}, w_{sol}) = \phi_{exp}$, we determine the linear crack number density $\lambda_{L\text{-}sol}$ satisfying this equality.

4. Finally, using equation (11), and setting $k_{eff}(\lambda_{L\text{-}sol}, w_{sol}/R_{sol}, w_{sol}) = k_{exp}$, we determine the effective crack radius R_{sol} satisfying this equality.

5. Knowing w_{sol} and R_{sol}, we compute the effective aspect ratio of the cracks $\xi_{sol} = w_{sol} / R_{sol}$.

This strategy is implemented considering the permeability values estimated at room conditions in the range 1 to 5 μD and a porosity of either ϕ = 0.8% (experimentally measured) or ϕ = 0.45% (determined from 2D microstructure). Table 1 summarizes the results of the data inversion using these input parameters.

run #	ϕ (%)	k (10^{-18} m²)	w (nm)	λ_L (m^{-1})	R (μm)	ξ
1	0.8	1	29	99009	none	none
2	0.8	5	65	44173	none	none
3	0.45	1	39	73622 (ρ_V ~ 0.032)	0.92	4.2 x 10^{-2}
4	**0.45**	**5**	**87**	**33003 (ρ_V ~ 0.025)**	**2.6**	**3.3 x 10^{-2}**

Table 1. Results of the data inversion from effective medium modeling.

For the first two scenarios (run #1 and #2) in Table 1 we observe that no value of the effective crack radius R can satisfy ϕ = 0.8% and k = 1 μD, or ϕ = 0.8% and k = 5 μD. The derived aperture w and linear crack number density λ_L do not match the corresponding parameters estimated from 2D microstructural analysis (w_{micro} ~ 140 nm and $\lambda_{L\text{-}micro}$ ~ 14724 m^{-1}).

The two other scenarios (run #3 and #4) yield reasonable results, that is,

- An effective crack radius exists (R = 0.92 to 2.6 μm) that honors the measured permeability ($k = k_{exp}$ = 1 to 5 μD) and porosity ($\phi = \phi_{micro}$ = 0.45%)
- The inverted apertures (w_{sol} = 39 to 87 nm) do not match the corresponding parameter estimated from 2D microstructural analysis (w_{micro} ~ 140 nm and $\lambda_{L\text{-}micro}$ ~ 14724 m^{-1}). However, out of all scenarios, #4 (ϕ = 0.45% and k = 5 μD) offers the value of half-aperture (w = 87 nm) closest to that determined from 2D microstructural analysis (w = 140 nm).
- The inverted crack number densities (λ_L=33003 to 73622 m^{-1}) do not match the corresponding parameter estimated from 2D microstructural analysis (λ_L ~14724 m^{-1}). However, out of all scenarios, #4 (ϕ = 0.45% and k = 5 μD) offers the value of crack number density (λ_L = 33003 m^{-1}) closest to the value determined from 2D microstructural analysis (λ_L = 14724 m^{-1}).
- The inverted crack aspect ratio (ξ = 3.3 to 4.2 10^{-2}) reflects a realistic crack geometry ($\xi << 1$).

In conclusion, scenario #4 is the most realistic in view of the available experimental and microstructural data. To generate this scenario, we have used as an input $k = k_{exp}$ = 5 mD and

$\phi = \phi_{micro} = 0.45\%$. The model and data inversion strategy outputs are: an effective half-aperture $w \sim 90$ nm, an effective crack radius $R \sim 2.6$ μm, an effective aspect ratio $\xi \sim 3\times10^{-2}$ and a crack number density $\lambda_L \sim 33003$ m^{-1} (or crack density $\rho_V \sim 0.025$).

Although the inverted w, R, ξ, and λ_L are not exactly those determined from the microstructural analysis, they are reasonably close, and most importantly, they yield the expected porosity and permeability. The discrepancies can be explained as follows:

- The difference in crack aperture (90 nm versus 140 nm) could be due to (i) the resolution limits of the 2D image; (ii) an undesired inflation of the cracks after Wood's metal injection; and/or (iii) the use of 2D images to determine a 3D parameter.

- The difference in crack number density (33003 m^{-1} versus 14724 m^{-1}) could be due to the heterogeneity of the rock and the fact that the images probe only a sub-volume (in fact a 2D surface) of the whole sample on which the porosity/permeability are measured.

- The difference between the measured porosity (0.8%), and the porosity determined from 2D microstructures (0.45%) could be due to: (i) the heterogeneity of the rock and the fact that the images probe only a sub-volume (in fact a 2D surface) of the whole sample on which the porosity/permeability are measured, and/or (ii) a resolution limit of the porosity measurement as this type of crack porosity is inherently very small.

- The inverted crack radius $R \sim 2.6$ μm does not seem to qualitatively reflect the scale of the cracks highlighted by Wood's metal injection in Figure 5; in the figure, the cracks appear longer than 2.6 μm. However, the effective crack radius is determined from the effective hydraulic permeability of the rock which hosts natural and jagged cracks, perhaps with multiple contact points between asperities (see Sarout et al. (2017)), so that the effective hydraulic radius is smaller than the cracks length visualized in the 2D thin section. Other possible causes of discrepancy listed above could also contribute to the discrepancy in the inverted crack radius. For instance, the injection of Wood's metal could have inflated the crack network so that the cracks appear thicker (larger aperture), and longer (less contacts at asperities).

4.4 Permeability Estimation from Percolation Model (MICP)

MICP results from the Grimsel granodiorite can be used with the Katz and Thompson equation (Katz & Thompson, 1986) as outlined in (Hu et al., 2015). This model is based on percolation theory and states that a critical pore (or crack) size controls permeability. The critical pore size can be determined from the inflection point of the MICP cumulative intrusion curve when mercury starts to percolate into the pore space. According to this model, the permeability k is given by:

$$k = \frac{1}{89}(d_{max})^2 \left(\frac{d_{max}}{d_C}\right) \phi S(d_{max}) \quad (13)$$

where d_{max} is the pore throat diameter at which conductance is maximum, d_C is the critical

pore throat diameter at percolation threshold and $S(d_{max})$ is the mercury saturation at a pressure corresponding to d_{max} (Hu et al., 2015). Using the throat size distribution given in Figure 7 and the porosity derived from MICP on the same plug, a predicted permeability value of 1.05 10^{-18} m² for the unstressed rock is obtained, suggesting that MICP captures the correct characteristics of the fluid flow pathways at the sample scale.

4.5 Permeability Estimation from Free-Fluid Model (NMR)

NMR analysis is also able to predict the permeability from the T_2 relaxation time distribution (Josh et al., 2012) shown in Figure 8. In this analysis permeability prediction is based on the free fluid model by Coates et al. (1991). As the five samples were first measured saturated then desaturated after centrifuging, one can estimate the Free Fluid Index *FFI* (corresponding to the water removed at 6.9 bars equivalent capillary pressure) and the Bound Volume Index *BVI* (corresponding to irreducible water). Saturated and desaturated samples help to define the T_2 cutoff that separate *FFI* from *BVI* as shown in the example on sample X1 (Figure 12a). The five samples record a T_2 cutoff around 30 ± 10 ms, very close to values found in the literature for quartz rich rocks (around 33 ms).

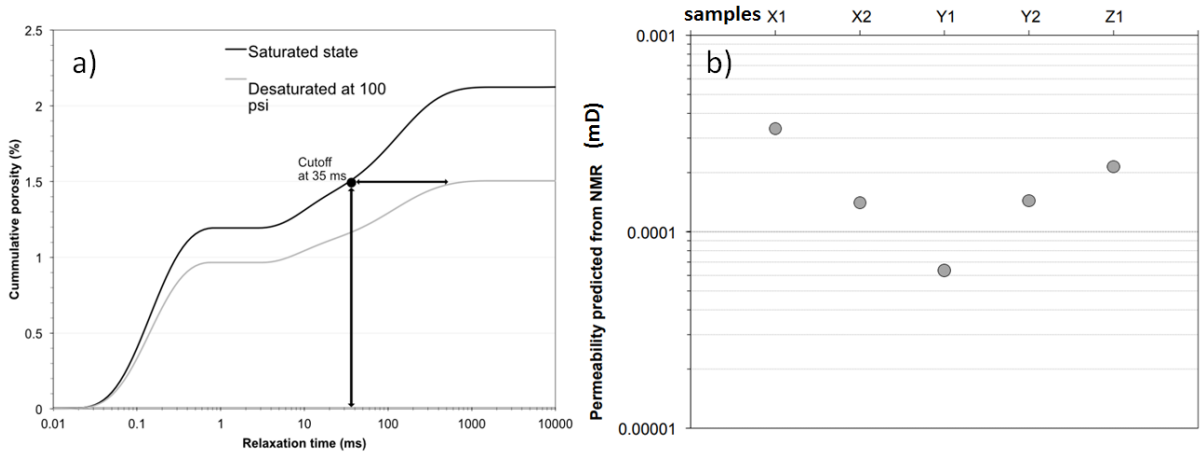

Figure 12. a) Example of NMR cumulative porosity of sample X1 under saturated and desaturated conditions to measure the T_2 cutoff that separates mobile and irreducible water. b) Predicted permeability from NMR in five small core plugs of Grimsel granodiorite using classical parameters from Coates.

As formulated in the Coates model (Coates et al., 1991), the NMR predicted permeability is given by:

$$k = \left(\frac{\phi}{\Gamma}\right)^4 \left(\frac{FFI}{BVI}\right)^2 \quad (14)$$

where Γ is a constant related to pore geometry. Using a standard value for Γ according to the Coates model (Γ=10 when the permeability unit is mD (10^{-15} m²) and porosity is in %, the five tested plugs have a predicted permeability ranging from 0.14 to 0.35 10^{-18} m² (average 0.20 10^{-18} m²) except for sample Y1, which has a lower permeability (0.063 10^{-18} m²)(Figure 12b). These values are lower than the average permeability found in the benchmark (see companion paper). However they were obtained at 13 MPa confining pressure whereas the KG^2B effective pressure target was 5 MPa. Taking into account the pressure dependence of permeability shown in the companion paper, the NMR predicted permeability values are in

good agreement with the measured permeability range.

4.6 Permeability Estimation from RC Filter Analog

Here we report a new way to analyze the data generated by pore fluid pressure oscillation experiments (see companion paper) based on modeling the rock as a RC filter. The approach has been used by Mckernan et al. (2017) and Rutter and Mecklenburgh (2018). In contrast to the four previous models, this model is based on a physical analog rather than microstructural data. Oscillatory flow of fluid through the pores of a rock is analogous to the flow of electricity through a resistor-capacitor network. A first order resistance-capacitance (RC) filter is shown in Figure 13a. This corresponds to a rock sample (the resistive element) of zero storativity (zero porosity), and the downstream reservoir corresponds to the capacitive element. The transfer function or gain $G=V_{out}/V_{in}$ depends on the frequency f because of the time required to charge the capacitor through the resistor. At low frequencies the capacitor is infinitely resistant so a waveform applied as V_{in} passes unimpeded (provided the output does not draw current). Beyond the break frequency f_B the capacitor can conduct so the R and C elements form the arms of a potential divider and the output is progressively attenuated as frequency is increased. This is a low pass filter, because the unattenuated frequencies are low frequencies. The high frequency waveform amplitude attenuation rate (gain) is always 20 dB per decade; it has a slope of -1 on a plot of log G vs log f. The linear prolongation of the high frequency slope intersects the gain = 1 abscissa at a characteristic break frequency (or corner frequency) $f_B = 1/(2\pi RC)$. The output (across the capacitor) of an RC filter also has a particular response to a step change in input voltage, with v_{out} decaying exponentially with time. This was the basis of the widely-used pulse transient decay method proposed by Brace et al. (1968) for the measurement of permeability of tight rocks.

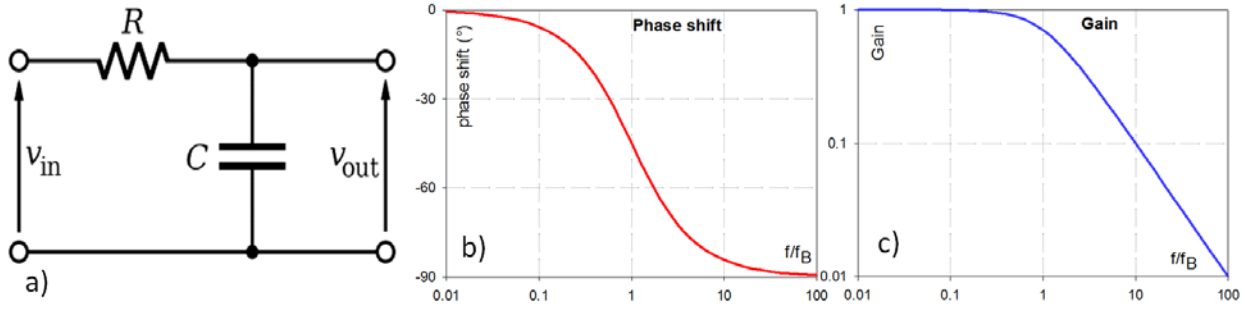

Figure 13. a) A first order electrical low pass filter analogous to fluid flow through a resistant rock R of zero storage capacity, with a capacitor C analogous to the downstream storage reservoir. Variation of b) phase shift and c) gain A with applied waveform frequency for a low pass electrical filter.

In addition to progressively attenuating the output waveform, the filter progressively shifts its phase over the frequency range between the two linear segments, from 0° to 90° (Figure 13b). The gain G and phase shift θ can be expressed respectively as:

$$\boldsymbol{G = \frac{V_{out}}{V_{in}} = \frac{1}{\sqrt{1+(f/f_B)^2}}} \quad (15)$$

$$\boldsymbol{\theta = -\tan^{-1}\left(\frac{f}{f_B}\right)} \tag{16}$$

Higher-order low-pass filters can be formed by cascading first order filters to simulate the behavior of more porous rocks (higher storativity). A rock might be imagined as a series of such filters, with capacitive components corresponding to pore spaces connected by resistors that combine to form the total resistance to flow. Each RC element in series can apply an additional phase shift, but many such phase shifts will result in severe attenuation. Many possible topologies of R and C combinations can be imagined, with the final capacitor corresponding to the downstream volume of the permeameter. Analysis of such combinations is beyond the scope of the present paper. Smaller ratios of rock storativity to downstream storage translate to smaller phase shifts for a given gain, so that the behavior more closely resembles that of a first-order filter.

This approach was evaluated on a Grimsel granodiorite sample cut at a high angle to the foliation (called hereafter core C), to investigate how similar its behavior is to that of an RC filter. Pore fluid pressure oscillation tests were conducted with a pressure cycling period ranging from 50 to 12800 seconds (i.e. 7.8 10^{-5} s^{-1} < f < 2 10^{-2} s^{-1}). Figure 14a shows a plot of log G vs log f for the driving waveform when total confining pressure is 20.0 MPa and pore pressure is 15.5 MPa. As expected the behavior is similar to that of an RC filter with log f_B = -2.869 (i.e. f_B=1.35 10^{-3} s^{-1}). The slope in the frequency-dependent region is -1.16, slightly greater than unity, as might be expected for the small degree of storativity (non-zero porosity) within the rock specimen.

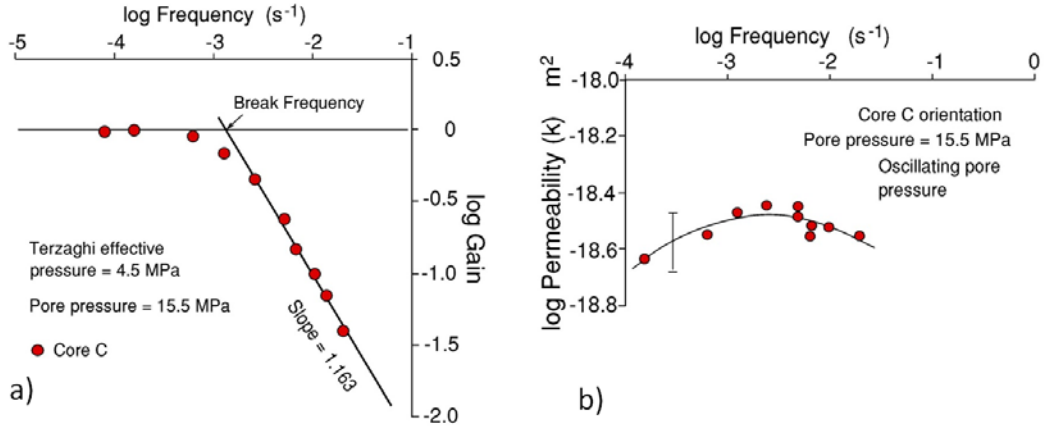

Figure 14. a) Plot of log G versus log f for core C at 4.5 MPa effective pressure and 15.5 MPa pore pressure of argon gas. This is typical of rock behavior as a first order filter with very small storativity in the rock sample (slope of -1.16 close to unity). b) Frequency dependence of permeability calculated for the individual data. The peak in the convex upward curve corresponds to the break frequency. The average of the log k data lying above the break frequency is -18.52.

The fluid flow analogs of resistance R and capacitance C are:

$$\mathbf{R} = \frac{\boldsymbol{L\mu}}{\boldsymbol{Ak}} \text{ and } \mathbf{C} = \boldsymbol{\beta_D} \tag{17}$$

where L and A are the length and cross-sectional area of the sample respectively, and β_D is the storage of the downstream reservoir (m^3/Pa). Permeability can therefore be calculated from the break frequency provided that the frequency-dependence of gain is measured at constant confining pressure and pore pressure conditions:

$$k = 2\pi\mu(L/A)\beta_D f_B \quad (17)$$

This yields log k = -18.33 (i.e. k=0.47 10^{-18} m²) for the tested sample. Leaving aside the most extreme values of very small or very large gain, the average of all the individual permeability measurements is log k = -18.52 ± 0.06 (k=0.30 10^{-18} m²). The plot of log k vs log f (Figure 14b) shows slight upward convexity, similar to what was found for a sandstone by Song and Renner, (2007). One of the KG²B labs (Lab#18, see companion paper) measured a permeability of 0.501 10^{-18} m² on this sample with the standard approach for analyzing pore pressure oscillation tests (Bernabé et al., 2006), and 0.582 10^{-18} m² using a transient pulse test.

5. Complementary Outcome of the Benchmarking Exercise

In this section we present additional data produced by the KG²B team in their study of the Grimsel granodiorite core samples. This data set is not as exhaustive as the permeability data set because it was done on a voluntary basis with no specific instructions.

5.1. Permeability – Porosity Relationship

A log-log plot of permeability vs. porosity (Figure 15) shows a general trend with two outliers and one isolated point aligned with the general cloud consistent with the expected trend of permeability decrease with decreasing porosity. The correlation is not very strong, which is not really surprising as permeability is controlled by the geometrical properties (pore size and shape, topology and connectivity) of the 3D pore or crack network and not simply by the bulk porosity. Nevertheless, a simple power-law can be fitted to the data set (minus two outliers) with an exponent equal to 2 (Figure 15). The sample in the lower left corner was considered as an outlier in the statistical analysis presented in the companion paper: its low permeability can be explained by its porosity being much lower than all the others. A power-law relationship between permeability and porosity has often been invoked (e.g. David et al., 1994 and references therein). Wang et al. (2016) found an exponent between 4 and 5 in their permeability-porosity correlation for two granite gneiss samples. In our KG²B experiments, porosity was measured at room conditions whereas permeability was measured at 5 MPa effective pressure. If both properties were measured under the same pressure conditions, the correlation would probably have been better.

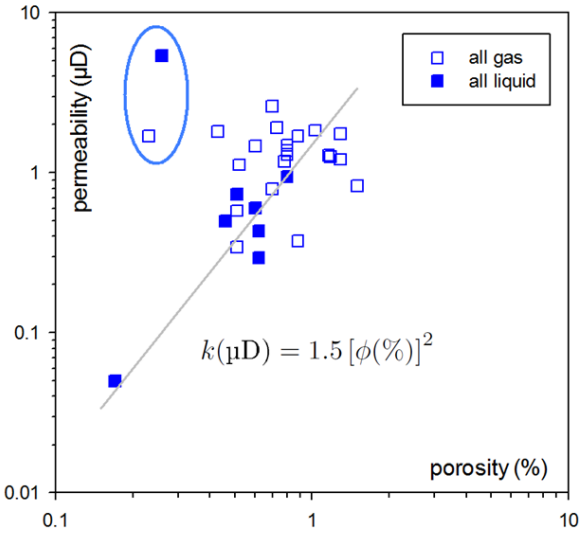

738

739 **Figure 15.** Correlation between permeability and porosity.

740

741 ## 5.2. Permeability Anisotropy

742 Three participants (Lab#8, Lab#18 and Lab#22) reported permeability measurements
743 in more than one direction in order to test for permeability anisotropy. These data sets include
744 the one presented in section 4.6. which was obtained by Lab#18 using the oscillating pore
745 pressure method and supplemented with measurements made in two other directions using
746 the transient pulse method. The two other labs used the steady state and the transient pulse
747 methods. All the anisotropy data was obtained using gas as the flowing fluid. The results are
748 compiled in Figure 16, together with those from *(*Schild et al., 2001). For the KG²B core, an
749 orientation nomenclature was adopted whereby *Ax* represents the direction parallel to the core
750 axis, *D1* is the direction perpendicular to *Ax* and parallel to the foliation; and *D2* is
751 perpendicular to both *Ax* and *D1*. Note that *D2* is nearly perpendicular to the foliation (~70°).
752 Schild et al., (2001) investigated permeability parallel and perpendicular to the foliation and
753 for the sake of comparison those directions were associated with directions *D1* and *D2*,
754 respectively. Overall, anisotropy emerges from the comparison between directions *D1* and
755 *D2*, where the permeability along the foliation consistently measures higher than the one
756 (quasi-) perpendicular to it (respective anisotropy coefficients of ~50% and ~60% for the
757 OSC and PLS measurements of Lab #18). This result is qualitatively consistent with the data
758 of Schild et al., (2001), albeit over a greater range of anisotropy coefficients. It also compares
759 well with the velocity data of Schild et al., (2001) and the velocity measurements made
760 during our screening of the KG²B plugs (~30% P-wave anisotropy reported in (David et al.,
761 2017)).

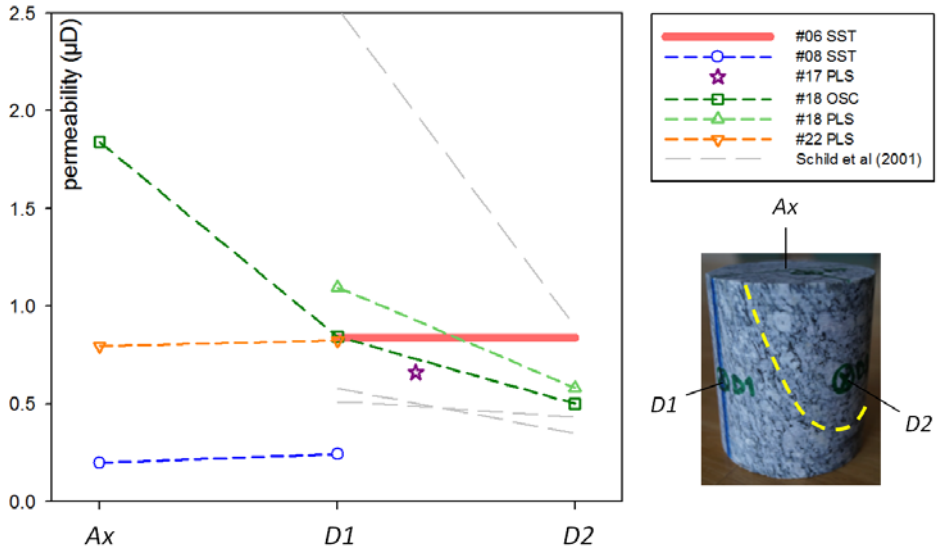

Figure 16: Permeability measured in direction *Ax*, along the core axis, *D1* parallel to the foliation and *D2* nearly perpendicular to the foliation. The grey lines are data published in Schild et al. (2001).

When both *D1* and *D2* plugs were tested, the permeability nearly perpendicular to foliation (along *D2*) was systematically smaller that in the direction nearly parallel to foliation (along *D1* or *Ax*). Little permeability anisotropy was expected to arise from the measurements made along *Ax* and *D1*, as *Ax* is relatively close to the foliation. This is confirmed by the results of Lab#08 and Lab#22. The value obtained along *Ax* by Lab#18 is not consistent with that picture; it might be attributable to heterogeneity from sample to sample. More specifically, since permeability is considered as being largely controlled by micro-cracking in the biotite grain fraction, slight changes in biotite content and grain size from sample to sample could result in large baseline contrasts. A better assessment could be obtained if the same representative elementary volume was measured along several directions as opposed to distinct plugs of various dimensions. Two additional participants (Lab#6, Lab#17) measured the permeability only in radial directions: both values fall in the range of radial permeability found by the others. The sample tested by Lab#17 was oriented at about 30° from the foliation, and the radial permeability measured by Lab#06 is an average one (plotted with an horizontal line) derived from a radial water flow experiment on a hollow cylinder parallel to the core axis (Monfared et al., 2011) at 1.75 MPa effective confining pressure, lower than the KG2B target. Due to the limited number of samples, the anisotropy analysis is far from being as convincing as the general KG²B data set.

5.3. Poroelastic Parameters

In situ rock masses include pore, crack, fracture networks which are usually saturated or partially saturated with fluids, often with 2 or more fluid phases such as gas, water, or oil. The degree of saturation, ranging between 0 and 1, is the ratio of volume of pore fluid in the pore space to the pore volume. Controlling saturation during laboratory tests is important for two main reasons: i) to reproduce field conditions; ii) for intrinsic permeability estimates. For the latter purpose, full saturation of specimens with fluid used for measurement is essential (Zinszner & Pellerin, 2007). For measurements using gas, particular attention has to be paid to sample preparation and drying. For permeability measurement using liquids, key issues include expelling trapped gas and checking for full saturation with liquid phase. For measurement with water, flushing of de-aired water into the specimen, followed by a step by step back pressure increase, have been recommended in order to avoid additional gas entry

and to force trapped gas into solution (Black and Lee, 1973). This method was successfully applied to a tight porous rock, the Opalinus clay (Wild et al., 2015) and also in the present study by Lab#04 on a Grimsel granodiorite sample. Between each back pressure step, the poroelastic response to hydrostatic confinement was checked in order to assess the degree of saturation. The isotropic Skempton's coefficient measurements, defined as $B=\Delta P_p/\Delta P_c$, the ratio of pore pressure change to confinement pressure change, should reach a plateau when all trapped gas bubbles are dissolved in the solution. For the Grimsel granodiorite initially filled with water under vacuum, a plateau is reached when the pore pressure exceeds about 1.8 MPa (Figure 17a), and the "saturated" Skempton's coefficient is B=0.89 at 0.25 MPa effective confining pressure.

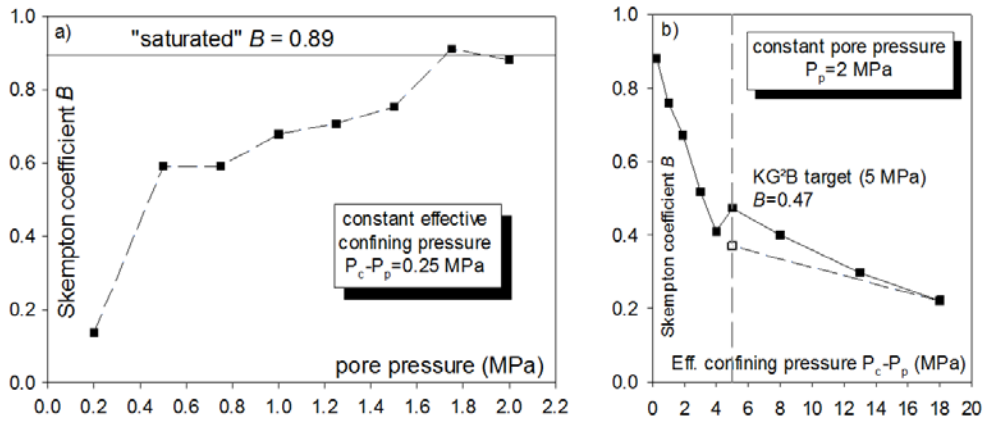

Figure 17. a) Evolution of the Skempton's coefficient B vs. pore pressure. b) Evolution of the Skempton's coefficient B vs. effective confining pressure at constant pore pressure (2 MPa).

Once the "saturation" pore pressure was reached, the confining pressure was increased at constant pore pressure (P_p=2 MPa) to the KG²B pressure target (P_{eff} = 5 MPa) and beyond. The increase of effective confining pressure resulted in a sharp drop of the Skempton's coefficient (Figure 17b) to 0.47 at the target pressure, and even lower at higher pressures. This behavior is probably linked to the progressive closure of cracks in the rock sample.

Another poroelastic parameter was determined by one of the participants (Lab#19), the Biot-Gassmann effective pressure coefficient α. This coefficient was obtained from several permeability measurements under different pressure conditions (both P_p and P_c). The effective pressure law $P_{eff} = P_c - \alpha P_p$ was established for permeability, and it was shown that the effective pressure coefficient α was equal to 1 (see companion paper).

6. Discussion

To complement the experimental permeability data set presented in the companion paper, we present additional data from microstructural analyses using BIB-SEM and micro-CT, as well as permeability predictions from various models. High quality imaging with BIB-SEM technology allowed us to identify pores and cracks at the micrometer scale and their relation with the rock mineralogy. Most of the cracks are located within biotite or at grain boundaries. The Wood's metal injection technique, combined with SEM, provided detailed and realistic images of the actual crack network, its connectivity (from which an average coordination number can be estimated) and tortuosity. A statistical analysis provided relevant

data on pore size, crack length and aperture, and porosity obtained from more than 60,000 elements; the amount and quality of these data provided valuable information for permeability modeling. Micro-CT imaging provided 3D volume rendering of the matrix density as well as a 3D map of pore locations. Two important conclusions could be drawn: (i) at the sample scale, the material appears to be very heterogeneous, with the size of heterogeneities exceeding the sample size and (ii) the pores resolved by micro-CT are isolated, confirming that fluid flow is controlled by a network of submicron cracks. It seems clear that the size of the samples studied (core sample with 4 mm diameter and 10 mm length) is well below the REV, which may explain the larger scatter in measured permeability values for small samples shown in the companion paper.

Table 2 summarizes the results of permeability modeling using microstructural data as input parameters. For each model, a short description is provided, and the input parameters are given.

MODEL	DESCRIPTION	INPUT PARAMETERS	PERMEABILITY PREDICTION
Statistical model	3D array of orthogonal intersecting cracks with same length and aperture	porosity, mean crack aperture	k_{pred} = 30 10^{-18} m²
Statistical model (Zimmermann et al., 2005)	array of parallel cracks with the same aperture	linear density of cracks, mean crack aperture	k_{pred} = 28 10^{-18} m²
Percolation model (Katz & Thompson, 1986)	based on the estimation of the critical crack aperture at percolation threshold	MICP intrusion volume vs. pressure graph, pore throat and saturation at threshold pressure, porosity	k_{pred} = 1.1 10^{-18} m²
Free-fluid model (Coates et al., 1991)	based on NMR relaxation time distribution	NMR T_2 spectrum, porosity, free and bound water fractions	0.13 10^{-18} m² < k_{pred} < 0.33 10^{-18} m² (@13 MPa)
Pore network model (David, 1993 Casteleyn et al., 2011)	3D cubic network of pipes with elliptical cross-section and constant length	crack aperture distribution from MICP, crack aspect ratio, porosity, fraction of occupied bonds χ	(χ=100%) k_{pred} = 28 10^{-18} m² (χ=53%) k_{pred} = 2.5 10^{-18} m² (χ=38%) k_{pred} = 0.25 10^{-18} m²
Effective medium model (Sarout et al., 2017)	3D random distribution of penny-shaped cracks	crack density, porosity, crack aperture, crack aspect ratio	k_{pred} = 5 10^{-18} m²

Table 2. Summary of permeability predictions obtained with 6 different models using input parameters based on microstructural data.

- Both statistical models yield a permeability value of about 30 10^{-18} m², significantly larger than the mean outcome for the measured permeability data set (~1 10^{-18} m²). These models are based on an oversimplified representation of the pore space where heterogeneity is absent, so that analytical solutions for permeability can be calculated. The predicted values are likely higher because the microstructural data were obtained on stress-free samples, whereas permeability measurements were obtained at 5 MPa effective confining pressure. However, if one takes into account the pressure

dependence of permeability shown in the companion paper, extrapolated permeability at zero effective pressure would give a value in the range 2-10 10^{-18} m², still lower than the permeability predicted by both statistical models. This discrepancy suggests that the heterogeneous nature of the rock pore space is poorly accounted for in statistical models.

- In contrast, the percolation model proposed by Katz & Thompson (1986) takes advantage of the full mercury volume vs. pressure curve obtained in MICP experiments. This model postulates the existence of a subnetwork spanning the rock sample, consisting of highly conducting cracks with conductance larger than a critical value. Heterogeneity is taken into account, the model prediction of the model (~1 10^{-18} m²) is in good agreement with the measured permeability despite the fact that the effective pressures do not match. MICP coupled with percolation modeling provides the correct length scale for permeability estimation.

- Generally consistent results were obtained for NMR-predicted permeability using the free fluid model. This model is based on NMR detection of the fraction of bound water in the pore space. Although little information is captured regarding pore space geometry, the model was successful in predicting the correct range of permeability at the NMR operating confining pressure (13 MPa), based on the pressure dependence of permeability presented in the companion paper.

- The three-dimensional nature of fluid flow in porous rocks is accounted for in both the pore network model and the effective medium model. The difference between these models is the topology of the crack network: cracks are located at bonds in a cubic lattice for the former, and randomly distributed for the latter. For both models, the number of input parameters is larger: porosity, crack aperture and aspect ratio, length of pipes in the PNM and crack density in the effective medium model. Not all of these parameters are well constrained either by MICP or microstructural data. Therefore reasonable assumptions were made to find the best set of parameters to match permeability measurements at 5 MPa effective pressure. Interestingly, both models converge to a similar value of crack aspect ratio (~10^{-2}), an apparently reasonable value based on the micrographs in Figures 3 and 5. Another outcome of the pore network model is that a permeability prediction consistent with the measured value requires a coordination number close to three, again in agreement with the micrographs in Figures 3 and 5. However, the models disagree regarding crack length, of order 100 µm for the PNM, and 1 µm for the effective medium model. Whereas the former value corresponds more or less to the actual crack length imaged in Figure 5, the latter does not, and one may conclude that the effective medium model is unable to match all our observations. Nevertheless, as discussed in section 4.3, the discrepancy may be explained by the presence of asperities and the jagged nature of observed cracks; in the effective medium model, an actual crack might be viewed as a combination of smaller cracks relevant for fluid flow.

7. Conclusion

In the companion paper the complete data set of low-permeability measurements from a benchmarking exercise involving 24 laboratories was analyzed; here we present complementary results focusing on (i) quantitative analysis of microstructures and pore size

distributions, (ii) permeability modeling and (iii) measurements of permeability anisotropy and poroelastic parameters. BIB-SEM, micro-CT, MICP and NMR methods were used to characterize microstructures (both in 2D and 3D) and quantify pore size distribution. Wood's metal injection was used to image the crack networks on 2D images. All of these studies provided input parameters for permeability modeling using (i) basic statistical models, (ii) 3D pore network and effective medium models, (iii) a percolation model using MICP data and (iv) a free-fluid model using NMR data. A new method for simpler analysis of pore pressure oscillation tests, modeling the rock as an RC electrical circuit, was also described for the case of small sample storativity. The models were generally successful in predicting the observed range of measured permeability using microstructural, MICP and/or NMR data. Whereas statistical models overestimate the permeability due to lack of information on heterogeneity, percolation, pore network and effective medium models are more relevant and provide additional constraints on crack parameters such as aspect ratio, aperture, density and connectivity. This confirms that MICP and advanced microscopy techniques are potentially able to provide useful input data for permeability estimation. Additional results to complement the measured permeability data set show that (i) the average porosity measured on plugs is 0.77%+/-0.36%, (ii) a weak power-law with exponent 2 relates permeability to porosity, (iii) permeability measured ~orthogonal to foliation is lower that ~parallel to foliation, and (iv) the Skempton's coefficient at 5 MPa effective pressure is about 0.5. A second round of benchmarking is currently under way, with another tight material, the Cobourg Limestone. Additional challenges are expected in this benchmark, project called KCL as the permeability is in the nano-Darcy range (10^{-21} m²).

List of symbols

P_c, confining pressure (Pa)
P_p, pore pressure (Pa)
$P_{eff} = P_c - P_p$, effective pressure (Pa)
α, effective pressure coefficient
B, Skempton's coefficient
k, permeability (m^2)
k_{exp}, experimental value of permeability (m^2)
k_{pred}, predicted value of permeability (m^2)
k_{gas}, permeability measured with gas (m^2)
k_{liquid}, permeability measured with gas (m^2)
k_{eff}, predicted permeability given by the effective medium model (m^2)
T_2, NMR transverse relaxation time (s)
ϕ, porosity
ϕ_{micro}, porosity obtained from BIB-SEM analysis
w, average crack half aperture (m)
w_{sol}, effective crack half-aperture, solution of the effective medium model (m)
λ_L, linear crack density (m^{-1})
λ_A, surface crack density (m^{-2})
L_P, length of the pipes in the pore network model (m)
χ, fraction of occupied bonds in the pore network model
R, average crack radius (m)
R_{sol}, effective crack radius, solution of the effective medium model (m)
ξ, crack aspect ratio ($=w/R$)

942 ξ_{sol}, effective crack aspect ratio, solution of the effective medium model
943 N_V, number of cracks per unit volume (m^{-3})
944 V_C, volume of a single spheroidal crack (m^3)
945 $\rho_V = N_V.R^3$, crack density for effective medium model
946 m, hydraulic radius (m)
947 α, dimensionless parameter for Poiseuille's law (=1/3 for cracks)
948 *FFI*, free fluid index
949 *BVI*, bound volume index
950 Γ, constant linked to pore geometry in the free-fluid model
951 R, equivalent resistance in RC circuit
952 C, equivalent capacitor in RC circuit
953 $G=V_{out}/V_{in}$, gain
954 θ, phase shift (rad)
955 f, frequency (s^{-1})
956 f_B, break frequency (s^{-1})
957 L, sample length (m)
958 A, sample cross-sectional area (m^2)
959 μ, dynamic viscosity (Pa.s)
960 β_D, downstream reservoir storage (m^3Pa^{-1})
961 KG²B, K for Grimsel granodiorite benchmark
962 BIB-SEM, broad ion beam – scanning electron microscopy
963 ViP, Virtual Petroscan
964 PPL/XPL, in-plane / crossed polarized light
965 EDS, energy dispersive spectroscopy
966 PSD, pore size distribution
967 NMR, nuclear magnetic resonance
968 PNM, pore network modeling
969 WM, Wood's metal
970 MICP, mercury injection capillary pressure
971 REV, representative elementary volume
972 CT, computerized tomography

973

974 **Acknowledgments and Data Availability Statement**

975 This project was partially funded by a grant from the "Fondation de l'Université de Cergy-
976 Pontoise". We thank Belinda Godel for conducting the micro-CT study on a Grimsel
977 granodiorite sample at CSIRO Perth. The KG²B project is supported by the GIS Géosciences
978 Franciliennes (http://www.geosciences-franciliennes.fr) within the research group on "Low
979 Permeable Media". We thank Yves Bernabé and Steve Ingebritsen for their thorough early
980 review of both companion papers. All the data presented in this paper can be made available
981 upon request.

982

983 **References**

984 Abell, A. B., K. L. Willis, and D. A. Lange (1999), Mercury Intrusion Porosimetry and Image
985 Analysis of Cement-Based Materials, *J. Colloid Interface Sci.*, *211*(1), 39–44,
986 doi:10.1006/JCIS.1998.5986.

Baker, D. R., L. Mancini, M. Polacci, M. D. Higgins, G. A. R. Gualda, R. J. Hill, and M. L. Rivers (2012), An introduction to the application of X-ray microtomography to the three-dimensional study of igneous rocks, *Lithos*, *148*, 262–276, doi:10.1016/J.LITHOS.2012.06.008.

Bauer, D., S. Youssef, M. Fleury, S. Bekri, E. Rosenberg, and O. Vizika (2012), Improving the Estimations of Petrophysical Transport Behavior of Carbonate Rocks Using a Dual Pore Network Approach Combined with Computed Microtomography, *Transp. Porous Media*, *94*(2), 505–524, doi:10.1007/s11242-012-9941-z.

Bernabé, Y., C. Bruderer-Weng, and A. Maineult (2003), Permeability fluctuations in heterogeneous networks with different dimensionality and topology, *J. Geophys. Res. Solid Earth*, *108*(B7), doi:10.1029/2002JB002326.

Bernabé, Y., U. Mok, and B. Evans (2006), A note on the oscillating flow method for measuring rock permeability, *Int. J. Rock Mech. Min. Sci.*, *43*(2), 311–316, doi:10.1016/j.ijrmms.2005.04.013.

Black, D. K., and K. L. Lee (1973), Saturating Samples by Back Pressure, *J. Terramechanics*, *10*(2), 105, doi:10.1016/0022-4898(73)90019-0.

De Boever, E., C. Varloteaux, F. H. Nader, A. Foubert, S. Békri, S. Youssef, and E. Rosenberg (2012), Quantification and Prediction of the 3D Pore Network Evolution in Carbonate Reservoir Rocks, *Oil Gas Sci. Technol. – Rev. d'IFP Energies Nouv.*, *67*(1), 161–178, doi:10.2516/ogst/2011170.

Brace, W. F., J. B. Walsh, and W. T. Frangos (1968), Permeability of granite under high pressure, *J. Geophys. Res.*, *73*(6), 2225–2236, doi:10.1029/JB073i006p02225.

Casteleyn, L., P. Robion, C. David, P.-Y. Collin, B. Menéndez, N. Fernandes, G. Desaubliaux, and C. Rigollet (2011), An integrated study of the petrophysical properties of carbonate rocks from the "Oolithe Blanche" formation in the Paris Basin, *Tectonophysics*, *503*(1–2), 18–33, doi:10.1016/j.tecto.2010.09.031.

Coates, G. R., R. C. A. Peveraro, A. Hardwick, and D. Roberts (1991), The Magnetic Resonance Imaging Log Characterized by Comparison With Petrophysical Properties and Laboratory Core Data, in *SPE Annual Technical Conference and Exhibition*, Society of Petroleum Engineers.

David, C. (1993), Geometry of flow paths for fluid transport in rocks, *J. Geophys. Res. Solid Earth*, *98*(B7), 12267–12278, doi:10.1029/93JB00522.

David, C., Y. Gueguen, and G. Pampoukis (1990), Effective medium theory and network theory applied to the transport properties of rock, *J. Geophys. Res.*, *95*(B5), 6993, doi:10.1029/JB095iB05p06993.

David, C., T.-F. Wong, W. Zhu, and J. Zhang (1994), Laboratory measurement of compaction-induced permeability change in porous rocks: Implications for the generation and maintenance of pore pressure excess in the crust, edited by C. J. Marone and M. L. Blanpied, *Pure Appl. Geophys. PAGEOPH*, *143*(1–3), 425–456, doi:10.1007/BF00874337.

David, C., J. Wassermann, and The_KG^{2}B_Team (2017), The KG^{2}B Project: A World-Wide Benchmark of Low Permeability Measurement, in *Poromechanics VI*, edited by M. Vandamme, P. Dangla, J. M. Pereira, and S. Ghabezloo, pp. 1153–1161, American Society of Civil Engineers, Reston, VA.

Dillinger, A., and L. Esteban (2014), Experimental evaluation of reservoir quality in Mesozoic formations of the Perth Basin (Western Australia) by using a laboratory low field Nuclear Magnetic Resonance, *Mar. Pet. Geol.*, *57*, 455–469, doi:10.1016/j.marpetgeo.2014.06.010.

Egger, P. (1989), Study of excavation induced rock damage at the Grimsel Uderground Rock Laboratory, *Nucl. Eng. Des.*, *116*(1), 11–19, doi:10.1016/0029-5493(89)90199-4.

Fredrich, J. T., and T. Wong (1986), Micromechanics of thermally induced cracking in three crustal rocks, *J. Geophys. Res. Solid Earth*, *91*(B12), 12743–12764, doi:10.1029/JB091iB12p12743.

Gao, Z., and Q. Hu (2013), Estimating permeability using median pore-throat radius obtained from mercury intrusion porosimetry, *J. Geophys. Eng.*, *10*(2), 25014, doi:10.1088/1742-2132/10/2/025014.

Garboczi, E. J., K. A. Snyder, J. F. Douglas, and M. F. Thorpe (1995), Geometrical percolation threshold of overlapping ellipsoids, *Phys. Rev. E*, *52*(1), 819–828, doi:10.1103/PhysRevE.52.819.

Godel, B. (2013), High-Resolution X-Ray Computed Tomography and Its Application to Ore Deposits: From Data Acquisition to Quantitative Three-Dimensional Measurements with Case Studies from Ni-Cu-PGE Deposits, *Econ. Geol.*, *108*(8), 2005–2019, doi:10.2113/econgeo.108.8.2005.

Gueguen, Y., and J. Dienes (1989), Transport properties of rocks from statistics and percolation, *Math. Geol.*, *21*(1), 1–13, doi:10.1007/BF00897237.

Guéguen, Y., and V. Palciauskas (1994), *Introduction to the physics of rocks*, Princeton University Press.

Hadley, K. (1976), Comparison of calculated and observed crack densities and seismic velocities in westerly granite, *J. Geophys. Res.*, *81*(20), 3484–3494, doi:10.1029/JB081i020p03484.

Holzer, L., F. Indutnyi, P. Gasser, B. Munch, and M. Wegmann (2004), Three-dimensional analysis of porous BaTiO3 ceramics using FIB nanotomography, *J. Microsc.*, *216*(1), 84–95, doi:10.1111/j.0022-2720.2004.01397.x.

Hu, Q., R. P. Ewing, and S. Dultz (2012), Low pore connectivity in natural rock, *J. Contam. Hydrol.*, *133*, 76–83, doi:10.1016/J.JCONHYD.2012.03.006.

Hu, Q., R. P. Ewing, and H. D. Rowe (2015), Low nanopore connectivity limits gas production in Barnett formation, *J. Geophys. Res. Solid Earth*, *120*(12), 8073–8087, doi:10.1002/2015JB012103.

Jiang, M., J. Klaver, J. Schmatz, and J. L. Urai (2015), Nanoscale porosity analysis in

geological materials, in *Acta Stereologica, Proceedings 14th ICSIA, Liege, Belgium*.

Josh, M., L. Esteban, C. Delle Piane, J. Sarout, D. N. Dewhurst, and M. B. Clennell (2012), Laboratory characterisation of shale properties, *J. Pet. Sci. Eng.*, *88–89*, 107–124, doi:10.1016/j.petrol.2012.01.023.

Katz, A. J., and A. H. Thompson (1986), Quantitative prediction of permeability in porous rock, *Phys. Rev. B*, *34*(11), 8179–8181, doi:10.1103/PhysRevB.34.8179.

Klaver, J., G. Desbois, J. L. Urai, and R. Littke (2012), BIB-SEM study of the pore space morphology in early mature Posidonia Shale from the Hils area, Germany, *Int. J. Coal Geol.*, *103*, 12–25, doi:10.1016/j.coal.2012.06.012.

Klaver, J., S. Hemes, M. Houben, G. Desbois, Z. Radi, and J. L. Urai (2015), The connectivity of pore space in mudstones: insights from high-pressure Wood's metal injection, BIB-SEM imaging, and mercury intrusion porosimetry, *Geofluids*, *15*(4), 577–591, doi:10.1111/gfl.12128.

Kozeny, J. (1927), Uber kapillare Leitung der Wasser in Boden, *Sitzungs-ber. Akad. Wiss. Wien*, *136*, 271–306.

Mckernan, R., J. Mecklenburgh, E. Rutter, and K. G. Taylor (2017), Microstructural controls on the pressure-dependent permeability of Whitby mudstone, in *Geomechanical and Petrophysical Properties of Mudrocks, Geological Society of London Special Publication*, edited by E. Rutter, J. Mecklenburgh, and K. Taylor, p. 454.

Monfared, M., P. Delage, J. Sulem, M. Mohajerani, A. M. Tang, and E. De Laure (2011), A new hollow cylinder triaxial cell to study the behavior of geo-materials with low permeability, *Int. J. Rock Mech. Min. Sci.*, *48*(4), 637–649, doi:10.1016/j.ijrmms.2011.02.017.

Paterson, M. S. (1983), The equivalent channel model for permeability and resistivity in fluid-saturated rock—A re-appraisal, *Mech. Mater.*, *2*(4), 345–352, doi:10.1016/0167-6636(83)90025-X.

Rutter, E. H., and J. Mecklenburgh (2018), Influence of Normal and Shear Stress on the Hydraulic Transmissivity of Thin Cracks in a Tight Quartz Sandstone, a Granite, and a Shale, *J. Geophys. Res. Solid Earth*, *123*(2), 1262–1285, doi:10.1002/2017JB014858@10.1002/(ISSN)2169-9356.UPPERCRUST1.

Sarout, J. (2012), Impact of pore space topology on permeability, cut-off frequencies and validity of wave propagation theories, *Geophys. J. Int.*, *189*(1), 481–492, doi:10.1111/j.1365-246X.2011.05329.x.

Sarout, J., E. Cazes, C. Delle Piane, A. Arena, and L. Esteban (2017), Stress-dependent permeability and wave dispersion in tight cracked rocks: Experimental validation of simple effective medium models, *J. Geophys. Res. Solid Earth*, *122*(8), 6180–6201, doi:10.1002/2017JB014147.

Scherer, G. W., J. J. Valenza, and G. Simmons (2007), New methods to measure liquid permeability in porous materials, *Cem. Concr. Res.*, *37*(3), 386–397, doi:10.1016/j.cemconres.2006.09.020.

Schild, M., S. Siegesmund, A. Vollbrecht, and M. Mazurek (2001), Characterization of granite matrix porosity and pore-space geometry by in situ and laboratory methods, *Geophys. J. Int.*, *146*(1), 111–125, doi:10.1046/j.0956-540X.2001.01427.x.

Schmatz, J., J. L. Urai, M. Bublat, and T. Berlage (2010), PetroScan – Virtual Microscopy, in *Geophysical Research Abstracts*, p. EGU 2010-10061.

Schull, C. G. (1948), The Determination of Pore Size Distribution from Gas Adsorption Data, *J. Am. Chem. Soc.*, *70*(4), 1405–1410, doi:10.1021/ja01184a034.

Smith, P. A., W. R. Alexander, W. Kickmaier, K. Ota, B. Frieg, and I. G. McKinley (2001), Development and testing of radionuclide transport models for fractured rock: examples from the Nagra/JNC Radionuclide Migration Programme in the Grimsel Test Site, Switzerland, *J. Contam. Hydrol.*, *47*(2–4), 335–348, doi:10.1016/S0169-7722(00)00161-3.

Song, I., and J. Renner (2007), Analysis of oscillatory fluid flow through rock samples, *Geophys. J. Int.*, *170*(1), 195–204, doi:10.1111/j.1365-246X.2007.03339.x.

Song, Y., C. A. Davy, D. Troadec, A.-M. Blanchenet, F. Skoczylas, J. Talandier, and J. C. Robinet (2015), Multi-scale pore structure of COx claystone: Towards the prediction of fluid transport, *Mar. Pet. Geol.*, *65*, 63–82, doi:10.1016/j.marpetgeo.2015.04.004.

Song, Y., C. A. Davy, T. Nguyen Kim, D. Troadec, G. Hauss, L. Jeannin, and P. M. Adler (2016), Two-scale analysis of a tight gas sandstone, *Phys. Rev. E*, *94*(4), 43316, doi:10.1103/PhysRevE.94.043316.

Walsh, J. B. (1965), The effect of cracks on the uniaxial elastic compression of rocks, *J. Geophys. Res.*, *70*(2), 399–411, doi:10.1029/JZ070i002p00399.

Walsh, J. B., and W. F. Brace (1984), The effect of pressure on porosity and the transport properties of rock, *J. Geophys. Res.*, *89*(B11), 9425, doi:10.1029/JB089iB11p09425.

Wang, H. L., W. Y. Xu, M. Cai, and J. Zuo (2016), An Experimental Study on the Slippage Effect of Gas Flow in a Compact Rock, *Transp. Porous Media*, *112*(1), 117–137, doi:10.1007/s11242-016-0635-9.

Washburn, E. W. (1921), Note on a Method of Determining the Distribution of Pore Sizes in a Porous Material., *Proc. Natl. Acad. Sci. U. S. A.*, *7*(4), 115–116, doi:10.1073/pnas.7.4.115.

Wild, K. M., F. Amann, C. D. Martin, J. Wassermann, C. David, and M. Barla (2015), Dilatancy of clay shales and its impact on pore pressure evolution and effective stress for different triaxial stress paths, in *49th US Rock Mechanics / Geomechanics Symposium 2015*, vol. 4.

Wong, T.-F. (1982), Micromechanics of faulting in westerly granite, *Int. J. Rock Mech. Min. Sci. Geomech. Abstr.*, *19*(2), 49–64, doi:10.1016/0148-9062(82)91631-X.

Zimmermann, G., H. Burkhardt, and L. Engelhard (2005), Scale dependence of hydraulic and structural parameters in fractured rock, from borehole data (KTB and HSDP), *Geol. Soc. London, Spec. Publ.*, *240*(1), 37–45, doi:10.1144/GSL.SP.2005.240.01.04.

1145 Zinszner, B. and Pellerin, F.M. (2007), A geoscientist's guide to petrophysics, *IFP Publ.*, xxi,
1146 384 .

APPENDIX A

1148 [(3)]**The KG²B Team:** the benchmark involved 24 rock physics laboratories around the
1149 world. The name, e-mail addresses and institution of each participant and co-author are given
1150
1151 in Table A1.

PARTICIPANTS (alphabetic order)	E-MAIL	INSTITUTION
Alexandra AMANN HILDENBRAND / Bernhard KROOSS	alexandra.amann@emr.rwth-aachen.de	EMR group, Aachen University, Germany
Guillaume BERTHE / Marc FLEURY	guillaume.berthe@ifpen.fr	IFPen, France
Joël BILLIOTTE	joel.billiotte@mines-paristech.fr	École des Mines de Paris, France
Christian DAVID / Jérôme WASSERMANN	christian.david@u-cergy.fr	Université Cergy-Pontoise, France
Catherine DAVY	catherine.davy@ec-lille.fr	Ecole Centrale de Lille, France
Pierre DELAGE / Philipp BRAUN	delage@cermes.enpc.fr	ENPC, France
Jérôme FORTIN	fortin@geologie.ens.fr	ENS Paris, France
David GRÉGOIRE / Laurent PERRIER	david.gregoire@univ-pau.fr	Université de Pau, France
Qinhong (Max) HU	maxhu@uta.edu	University of Texas, Arlington, USA
Eberhard JAHNS	jahns@gesteinslabor.de	Gesteinslabor, Germany
Jop KLAVER	jop.klaver@emr.rwth-aachen.de	Aachen University, Germany
Didier LASSEUX / Yves JANNOT / Alain SOMMIER	didier.lasseux@u-bordeaux.fr	I2M TREFLE, Bordeaux, France
Roland LENORMAND	roland.lenormand@cydarex.fr	Cydarex, France
David LOCKNER	dlockner@usgs.gov	USGS Menlo Park, USA
Laurent LOUIS / Gregory BOITNOTT	llouis@ner.com	New England Research, Vermont, USA
Claudio MADONNA / Florian AMANN	claudio.madonna@erdw.ethz.ch	ETH Zurich, Switzerland
Philip MEREDITH / John BROWNING / Tom MITCHELL	p.meredith@ucl.ac.uk	UCL Earth Sciences, UK
Franck NONO / Didier LOGGIA	nono@gm.univ-montp2.fr	Université Montpellier II, France
Peter POLITO	peter.Polito@jsg.utexas.edu	University of Texas, Austin, USA
Thierry REUSCHLÉ	thierry.reuschle@unistra.fr	EOST Strasbourg, France
Ernie RUTTER	ernie.rutter@manchester.ac.uk	Univ. Manchester, UK
Joël SAROUT / Lionel ESTEBAN	joel.sarout@csiro.au	CSIRO, Perth, Australia
Patrick SELVADURAI	patrick.selvadurai@mcgill.ca	McGill University, Canada
Tiziana VANORIO / Anthony CLARK	tvanorio@stanford.edu	Stanford University, USA